International Materials Reviews

ISSN: (Print) (Online) Journal homepage: https://www.tandfonline.com/loi/yimr20

A review of solution combustion synthesis: an analysis of parameters controlling powder characteristics

Ekaterina Novitskaya , James P. Kelly , Sarit Bhaduri & Olivia A. Graeve

To cite this article: Ekaterina Novitskaya , James P. Kelly , Sarit Bhaduri & Olivia A. Graeve (2020): A review of solution combustion synthesis: an analysis of parameters controlling powder characteristics, International Materials Reviews, DOI: 10.1080/09506608.2020.1765603

To link to this article: https://doi.org/10.1080/09506608.2020.1765603

Published online: 14 Jun 2020.

INTERNATIONAL MATERIALS REVIEWS
https://doi.org/10.1080/09506608.2020.1765603

A review of solution combustion synthesis: an analysis of parameters controlling powder characteristics

Ekaterina Novitskaya[a], James P. Kelly[a], Sarit Bhaduri [b] and Olivia A. Graeve [a]

[a]Department of Mechanical and Aerospace Engineering, University of California, San Diego, CA, USA; [b]Department of Mechanical, Industrial and Manufacturing Engineering, University of Toledo, Toledo, OH, USA

ABSTRACT

The solution combustion synthesis technique is a versatile method for the production of powders used in a variety of applications. It has been used to produce hundreds of compounds, thus demonstrating its versatility, especially for the preparation of oxides, and is now a workhorse technique in materials science. Its success resides in the ease of implementation, high-throughput, the versatility of chemistries, and capacity for the production of high-surface area powders. The main limitations of the technique include problems with powder agglomeration, possible lack of control of powder morphologies, and the presence of leftover organic impurities from incomplete combustion. In this contribution, we review the influence of a variety of factors of relevance for the technique, including the type of fuel, fuel-to-oxidizer ratio, and combustion temperature, as well as the presence of additives and other special considerations, with a particular focus on the crystallite size and particle size of the resulting powders.

ARTICLE HISTORY
Received 1 April 2018
Accepted 1 May 2020

KEYWORDS
Combustion synthesis; processing; nanomaterials; ceramics; agglomeration; dynamic light scattering; nanocrystals; powders

Introduction

The solution combustion synthesis process is a simple and versatile methodology used to produce ceramic powders for a variety of technologies, including solid oxide fuel cells, catalysts, gas sensors, actuators, UV-absorbents, and colouring agents (ceramic pigments), among many others. The process consists of an exothermic chemical reaction between metal nitrates (oxidizers) and an organic fuel (e.g. carbohydrazide, urea, glycine, citric acid) mixed in the form of an aqueous (or rarely a non-aqueous) solution and subjected to relatively mild (300–500°C) heating, usually in a pre-heated muffle furnace. Key to the process is the atomic level mixing that is a result of the solubility of the precursors, which usually results in homogeneous powders. In many cases, synthesis needs to be followed by a calcination step to remove excess organic impurities from the as-synthesised powders. When necessary, the calcination step also serves to improve the crystallinity of the materials, as can be seen in Figure 1 for the synthesis of Y_2O_3, where (a) illustrates the X-ray diffraction pattern of powders in the as-synthesised state and (b) the powders after calcination at 1273 K for 12 h. The synthesis of a simple binary compound such as Y_2O_3 follows a reaction

$$Y(NO_3)_3 + \text{organic fuel} \longrightarrow Y_2O_3 + \text{gases} \quad (1)$$

in which the reactants are dissolved in a small amount of water and placed in a furnace or hot-plate at a pre-set furnace temperature. Within a few seconds, after the water evaporates, the nitrates and organic fuel react producing a mild or strong explosive reaction, depending on the fuel, with the release of heat and a variety of gases such as CO_2, NO_x, and CO, among others. Since the reaction is highly exothermic, nanocrystalline powders typically result as one of the products of reaction (see Figure 1(c)). During this type of combustion, also known as thermal explosion, the entire sample reacts simultaneously in a matter of seconds.

The general principles defining combustion synthesis, including thermal decomposition and energetics of the organic fuels, as well as processing parameters such as furnace temperature, fuel-to-oxidizer ratio, and adiabatic flame temperature, have been previously summarised by Shea et al. [1]. In addition, Mukasyan and Dinka [2] have discussed several different approaches to solution combustion synthesis, including self-propagating sol–gel combustion, conventional volume combustion synthesis, and the impregnated inert and impregnated active support modes. A variety of reviews on the combustion synthesis of oxide materials have been presented by Patil et al. [3] and Tyagi et al. [4,5], since oxides represent the great majority of materials prepared using this technique. However, it has been recently shown that the technique can also be used for the production of borides [6–10]. With respect to metals, Sharma et al. [11] have shown that pure silver particles can be synthesised by combustion synthesis using either citric acid or glycine, whereas

CONTACT Olivia A. Graeve ograeve@ucsd.edu http://graeve.ucsd.edu/ Department of Mechanical and Aerospace Engineering, University of California, 9500 Gilman Drive – MC 0411, La Jolla, San Diego, CA 92093-0411, USA

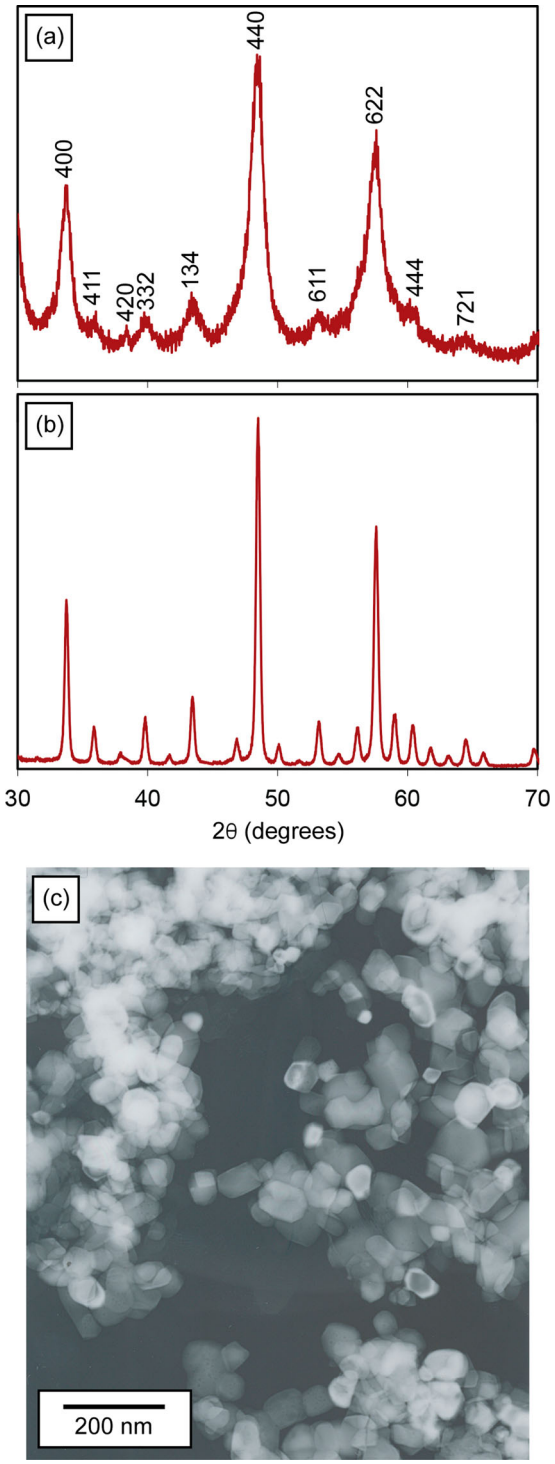

Figure 1. X-ray diffraction pattern of Y_2O_3 powders prepared by combustion synthesis (a) in the as-synthesised condition and (b) after calcination treatment at a temperature of 1273 K for 12 hr. (c) Transmission electron micrograph of Y_2O_3 powders prepared by combustion synthesis and calcined at 1273 K for 6 h.

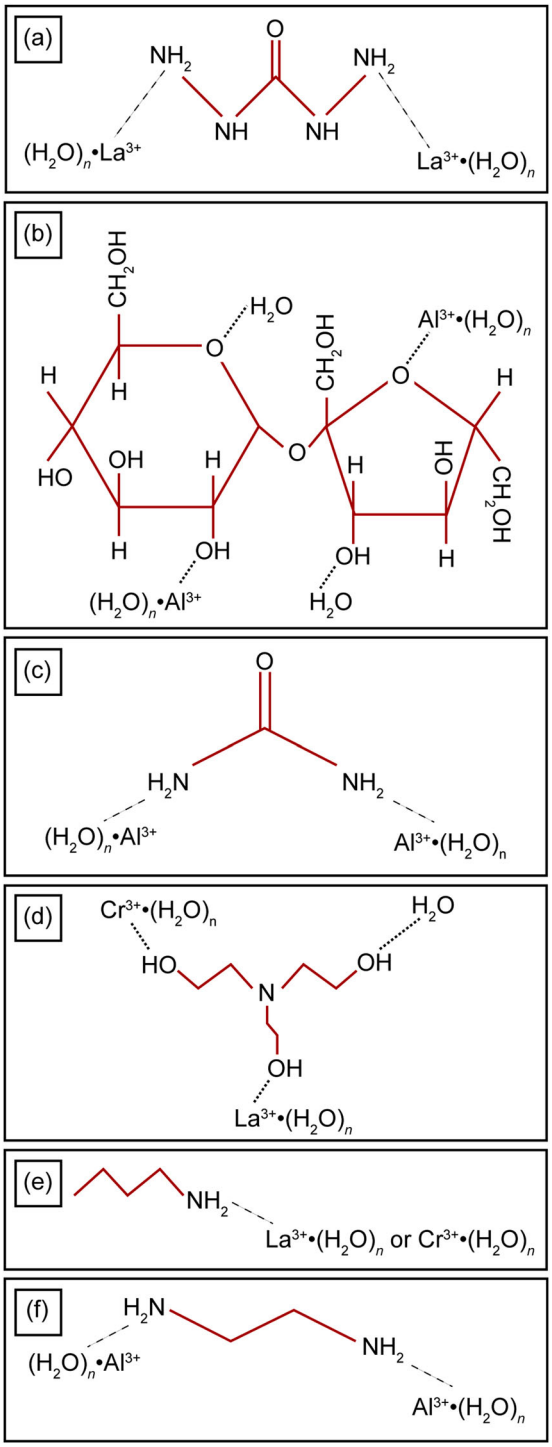

Figure 2. (a) Complex formation between dissolved La^{3+} ions and carbohydrazide for the synthesis of La_2O_3, (b) complex between dissolved Al^{3+} ions and sucrose for the synthesis of Al_2O_3 [14], (c) complex between dissolved Al^{3+} ions and urea for the synthesis of Al_2O_3 [14], (d) complex between dissolved La^{3+} and Cr^{3+} ions and triethanolamine for the synthesis of $LaCrO_3$ [15], (e) complex between dissolved La^{3+} and Cr^{3+} ions and *n*-butylamine for the synthesis of $LaCrO_3$ [15], and (f) complex between dissolved La^{3+} and Cr^{3+} ions and ethylenediamine for the synthesis of $LaCrO_3$ [15].

Zhu et al. [12] has reported the successful synthesis of small amounts of intermetallic $FeNi_3$ with citric acid.

The focus of this review is an analysis of the influence of synthesis parameters such as type and amount of fuel, temperature of the reaction, fuel-to-oxidizer ratio, and additives, on the final morphology of powders, with a particular emphasis on the effects of these parameters on the crystallite size and particle size. Specifically, the discussion is divided into the following sections: type of fuel (Section 2), fuel-to-oxidizer ratio (Section 3), pre-ignition temperature (Section 4), additives and other factors (Section 5), and challenges and limitations (Section 6).

Type of fuel

General considerations

This section will cover the main factors that influence powder morphology with respect to the type of fuel used during combustion. Depending on type (chemical composition) and amount of fuel, the actual combustion velocity and temperature can vary significantly, affecting the morphology and the size of the resultant powders. An optimum fuel is one that results in non-toxic gases ($H_2O + CO_2 + N_2$) by generating a complete combustion reaction, as well as serving as a complexant to the metal cations [13]. The complexation process increases the solubility of metal cations in water and prevents the premature precipitation of intermediate products and/or final products. For fuels with greater numbers of complexation sites, say sucrose (Figure 2(b)), the possibility for homogeneous dispersal of metal cations is improved. As an example, a combustion reaction between $La(NO_3)_3$ and the organic fuel carbohydrazide, results in a complex between carbohydrazide and the La^{3+} ions in solution, as illustrated in Figure 2(a) and described by

$$\begin{aligned} 2\ La(NO_3)_3 \ + \ a CH_6N_4O \ \longrightarrow \\ La_2O_3 \ + \ b H_2O + \ c CO_2 \ + \ d N_2 \\ + \ \text{other gases and/or radicals.} \end{aligned} \tag{2}$$

An example for the synthesis of γ-Al_2O_3 [14] using sucrose as fuel follows reaction

$$\begin{aligned} 2\ Al(NO_3)_3 \bullet 9H_2O(s) + x C_{12}H_{22}O_{11}(s) \ \longrightarrow \\ Al_2O_3(s) + a N_2(g) + b CO_2(g) + c H_2O. \end{aligned} \tag{3}$$

While an example for the synthesis of α-Al_2O_3 [14] using urea as fuel follows reaction

$$\begin{aligned} 2\ Al(NO_3)_3 \bullet 9H_2O(s) \ + \ x CH_4N_2O(s) \ \longrightarrow \\ Al_2O_3(s) + \ a N_2(g) \ + \ b CO_2(g) \ + \ c H_2O(g). \end{aligned} \tag{4}$$

The complexation processes for these two latter fuels are shown in Figure 2(b,c). The issue of solubility of reactants is important and the formation of aqueous complexes between the metal cations and the organic fuels is very relevant for the success of the process. Indeed, Ganesh et al. [14] attribute the smaller sizes of the sucrose γ-Al_2O_3 powders (crystallite size = 16 nm, particle size = 5.66 μm), compared to the larger sizes found for the α-Al_2O_3 urea powders (crystallite size = 98 nm, particle size = 7.22 μm), precisely to this effect.

Typical fuels used for combustion synthesis are illustrated in Figure 3. Fuels with longer molecular chains produce larger amounts of released gases during the process. Gas production and release can generally result in smaller crystallite sizes and less agglomerated powders because heat is dissipated from the system during gas ejection, reducing temperature and hindering crystal growth and agglomeration. From this perspective, fuels such as sorbitol, triethanolamine, and citric acid, would result in smaller crystallite and particle sizes. For example, Lakshmi et al. [16] showed that citric acid is better for producing scandia-stabilised zirconia powders of smaller crystallite sizes, while Rashad and El-Sheikh [15] demonstrated that $LaCrO_3$ powders can be produced using three organic fuels, namely triethanolamine (M_W = 149.19 g/mol), *n*-butylamine (M_W = 73.14 g/mol), and ethylenediamine (M_W = 60.10 g/mol), in order of decreasing chain length. The smallest and less agglomerated powders corresponded to triethanolamine, and the largest and most agglomerated powders corresponded to ethylenediamine. Also, larger fuels have more sites available to promote complex formation and solubility of metal cations, as seen in Figure 2(d) for the case of triethanolamine, compared to those for *n*-butylamine (Figure 2(e)) and ethylenediamine (Figure 2(f)). Thus, the effect of chain length (i.e. molecular weight) on the crystallite size and particle size is also connected to the solubility and complexation in fuels, not just to the release of gases.

Ghosh et al. [17,18] analysed the crystallite sizes and particle sizes of hydroxyapatite powders during synthesis using urea and glycine as fuels. Glycine has a slightly longer molecular chain length than urea but the calcium hydroxyapatite synthesised with glycine did not have the smaller particle size, rather the urea powders were smaller. As both glycine and urea are very similar in their molecular chain length, valuing chain length as the only parameter for crystallite size is not a complete descriptor. By means of comparison, Pacurariu et al. [19] showed that larger crystallite sizes for $MgAl_2O_4$ were produced for the fuel with longer molecular chain length (β-alanine) compared to the shorter molecular chain length (urea), whereas Deorsola and Vallauri [20] showed that ZnO and CeO_2 powders produced with citric acid (long chain) had larger crystallite sizes and higher agglomeration, while glycine and glycol (shorter chains) were the most optimised fuels for these materials [21,22]. Thus, a definite correlation between chain length and crystallite size cannot be established for some material systems, although it is a parameter that is useful as a first consideration, both from the point of view of gas release and complex formation for efficient dissolution of the reactant species. A more fundamental parameter is the heat of reaction, which is dependent on the number of single and double bonds in the different fuels. The fuels containing only single bonds between carbon atoms, such as glycine, alanine, polyethylene glycol, sorbitol, and hexamethylenetetramine, are known as saturated fuels. Those with double and triple bonds, such as urea, carbohydrazide, *n*-butylamine, ethylenediamine, triethanolamine, citric acid, acrylamide, and valine, are known as unsaturated fuels and are generally more reactive.

According to propellant chemistry, the molar ratio between fuel and oxidizer is based on the ratio between

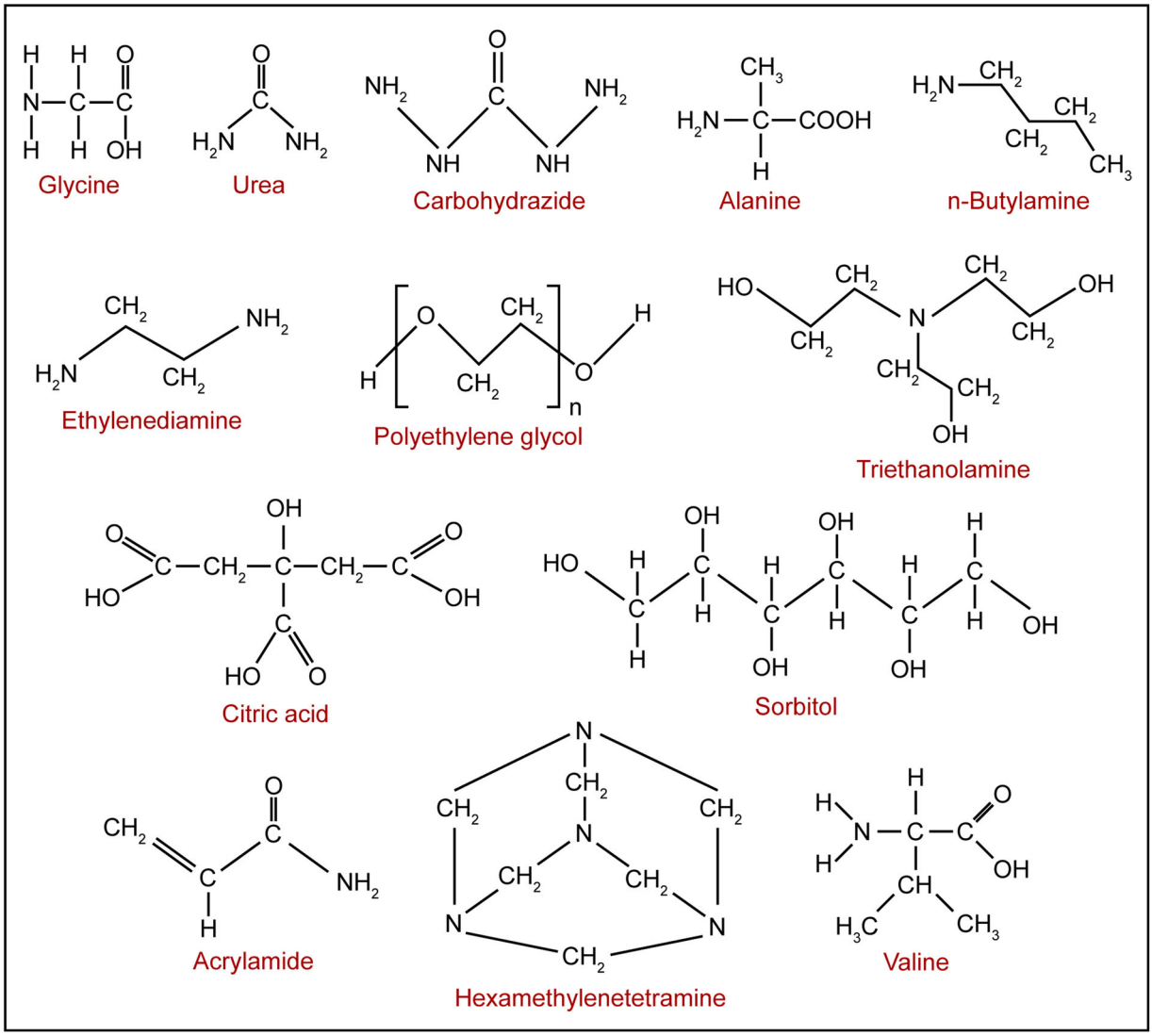

Figure 3. Common fuels used for combustion synthesis of nanocrystalline powders.

Table 1. Reducing valences of typical organic fuels used in solution combustion synthesis [13].

Fuel	Chemical formula	Reducing valence
Tryptophan	$C_{11}H_{12}N_2O_2$	−52
Sucrose	$C_{12}H_{22}O_{11}$	−48
Phenylalanine	$C_9H_{11}NO_2$	−43
Hexamethylenetetramine	$C_6H_{12}N_4$	−36
Arginine	$C_6H_{14}N_4O_2$	−34
Triethanolamine	$C_6H_{15}NO_3$	−33
Valine	$C_5H_{11}NO_2$	−27
n-Butylamine	$C_4H_{11}N$	−27
Sorbitol	$C_6H_{14}O_6$	−26
Glucose	$C_6H_{12}O_6$	−24
Glutamic acid	$C_5H_9NO_4$	−21
Ascorbic acid	$C_6H_8O_6$	−20
Citric acid	$C_6H_8O_7$	−18
Ethylenediamine	$C_2H_8N_2$	−16
Alanine	$C_3H_7NO_2$	−15
Acrylamide	C_3H_5NO	−15
Aspartic acid	$C_4H_7NO_4$	−15
Tartaric acid	$C_4H_6O_6$	−10
Ethylene glycol	$C_2H_6O_2$	−10
Glycine	$C_2H_5NO_2$	−9
Carbohydrazide	CH_6N_4O	−8
Urea	CH_4N_2O	−6
Hydrazine	N_2H_4	−4
Oxalic acid	$C_2H_2O_4$	−2

total oxidising valences (from the metal cations) and total reducing valences (from the fuel). The amount of fuel for every combustion reaction is fixed based on this ratio. The reducing valences of a variety of fuels were calculated by Shea et al. [13] and are listed in Table 1. A calculation between 1 mol of $M(NO_3)_3$ (M^{3+} = metal ion) and 1 mol of carbohydrazide, resulting in the −8 value given in Table 1, is as follows [23]

Oxidizing valences: (from the nitrate)

M: $1 \times (-3) = -3$

N: $3 \times (0) = 0$

O: $9 \times (2) = 18$

Total = 15

Reducing valences: (from the fuel)

H: $6 \times (-1) = -6$

N: $4 \times (0) = 0$

C: $1 \times (-4) = -4$

O: $1 \times (2) = 2$

Total = −8

The zero oxidising valence designated for N comes from the assumption that the product species is N_2, which may not be accurate since NO_x product species are also possible. In this scenario, the molar fuel to oxidizer ratio is then 8:15 = 8/15 = 0.53.

Heat of combustion

There are three main thermodynamic processes during combustion synthesis, namely heat generation as a consequence of the exothermic reaction, gas expulsion, and powder crystallization. All three of these processes affect the size of the resultant powders. In particular, a very high combustion temperature can result in the formation of relatively large crystallites of the desired powders, since the higher heat benefits crystal growth, a process that is controlled by diffusion of the reacting species and highly dependent on temperature *via* the following general Arrhenius description

$$g = g_o \exp\left[-\frac{\Delta E}{RT}\right], \quad (5)$$

where g is the growth rate, g_o is a temperature-independent constant, ΔE is the activation energy for crystal growth, R is the gas constant, and T is temperature. Gas expulsion, on the other hand, can reduce the temperature of the system by heat dissipation as a consequence of the escaping gases, hindering crystal growth. Thus, the heat of reaction and gas expulsion are competing effects. Unfortunately, the inherent reaction and formation of products during combustion synthesis are difficult to define because of the complexity of the chemical reactions inside the reaction zone. One can begin by defining an enthalpy of combustion, which can be described as the net increase in heat content when a substance in its standard state at ambient conditions undergoes complete oxidation. The simplest stoichiometric reaction follows a conversion from A to B (A → B), where A is an explosive mixture and B represents the products of detonation. Purohit et al. [24] described the formulation behind the estimation of the heat of combustion during synthesis, which can be calculated based on the following expression

$$\Delta H_{\text{combustion}} = (\Sigma\ \Delta H_f)_{\text{products}} - (\Sigma\ \Delta H_f)_{\text{reactants}}, \quad (6)$$

where $(\Sigma\ \Delta H_f)_{\text{products}}$ is the enthalpy of formation of the products and $(\Sigma\ \Delta H_f)_{\text{reactants}}$ is the enthalpy of formation of the reactants. One can see from Equation (6) that the enthalpy of combustion is described as a difference of enthalpies of formation between products and reactants. Thus, the amount of energy liberated during the combustion process is dependent on the starting reactants and resulting products, all of which must be determined in order to calculate the heat of combustion. For complex combustion reactions, products may be approximated, but not necessarily completely known. For example, in the simple reactions of Equations (1) and (2), the gases produced could include CO, CO_2, or both. In using

Table 2. Molar enthalpies of formation of several common fuels used in combustion synthesis.

Fuel	Chemical formula	Molar enthalpy of formation (kJ/mol)	Reference
Urea	CH_4N_2O	−333.3 ± 0.2	Dorofeeva et al. [26] and sources therein
		−333.4 ± 0.2	
		−320.2 ± 2.0	
		−333.1 ± 0.7	
		−333.1 ± 0.6	
		−333.4 ± 0.6	
		−333.6 ± 0.6	
		−333.1 ± 0.7	
		Average = −332	
Glycine	$CH_2(NH_2)COOH$	−530.1 ± 0.4	Dorofeeva et al. [26] and sources therein
		−537.2 ± 0.3	
		−528.6 ± 0.3	
		−527.5 ± 0.5	
		−528.5 ± 0.4	
		−528.1 ± 0.5	
		−524.0 ± 0.8	
		−528.1 ± 0.5	
		Average = −529	
Alanine	$CH_3CH(NH_2)COOH$	−604.2 ± 2.0	Dorofeeva et al. [26] and sources therein
		−562.7	
		−559.5 ± 0.6	
		−560.0 ± 1.7	
		−604.2 ± 2.0	
		−560.0 ± 1.0	
		Average = −575	
β-Alanine	β-$CH_3CH(NH_2)COOH$	−558.0	[27]
Valine	$HO_2CCH(NH_2)CH(CH_3)_2$	−628.9	[27]
Acrylamide	C_3H_5NO	−212.08	[27]
Polyethylene glycol	$C_{2n}H_{4n+2}O_{n+1}$	−3185.6	[28]
Sorbitol	$C_6H_{14}O_6$	−277.8	[28]
Citric acid	$C_6H_8O_7$	−1543.9	[21]
Glycol	$C_2H_6O_2$	−455.3	[21]
Hexamethylenetetramine	$C_6H_{12}N_4$	−205	[29]

carbohydrazide, one then obtains the following global reaction for the synthesis of Y_2O_3

$$2Y(NO_3)_3 + aCH_6N_4O \longrightarrow Y_2O_3 + bH_2O + cCO_2 + dN_2 \quad (7)$$

which defines the complete combustion and maximum release of energy between the oxidizer and the carbohydrazide fuel. However, under many circumstances, the following is a much better description of what transpires

$$2Y(NO_3)_3 + aCH_6N_4O \longrightarrow Y_2O_3 + bH_2O + cCO_2 + dN_2 + eCO + f\,NO_x + gH_2 + \text{other gases and/or radicals} \quad (8)$$

resulting in an incomplete combustion that also produces a variety of species from the dissociation of CO_2 and H_2O, possibly CO, H_2, O^{2-}, H^+, and OH^-, for example. Dissociation reactions are endothermic and result in a reduction in combustion temperature. Thus, as mentioned earlier, combustion reactions are complex and may include a series of individual steps that occur at different times during the detonation process, as well as endothermic reactions that reduce the temperature achieved by the system. Oxides of nitrogen can include nitrous oxide (N_2O), nitric oxide (NO) and nitrogen dioxide (NO_2)—NO_x is the general description for the mixture of NO and NO_2. One additional possibility is the formation of hydrogen cyanide (HCN), which can subsequently generate NO in the presence of oxygen. Oxidation and reduction reactions can also occur among products as described by

$$CO + H_2O \longrightarrow CO_2 + H_2, \quad (9)$$

$$2NO + 2CO \longrightarrow 2CO_2 + N_2, \quad (10)$$

$$2NO + 2H_2 \longrightarrow 2H_2O + N_2. \quad (11)$$

Table 2 summarises the molar enthalpies of formation of several common fuels, with polyethylene glycol and citric acid having the highest values. The difference in enthalpy of formation among the different fuels is one of the main reasons for the varied performance of these fuels during the combustion process since they produce different amounts of heat during the reaction. For example, Liao et al. [25] manufactured Tb-doped $Lu_3Al_5O_{12}$ powders using glycine (Figure 4(a)) and urea (Figure 4(b)). These two fuels have enthalpies of formation of −529 and −332 kJ/mol, respectively, representing the $(\Sigma\ \Delta H_f)_{reactants}$ in Equation (6). Thus, the enthalpy of combustion, $\Delta H_{combustion}$, is lower for the glycine fuel, resulting in smaller crystals for the glycine-produced powders, assuming all other factors can be ignored or minimised. Figure 4 shows this effect very clearly. The glycine-produced powders (Figure 4(a)) exhibit crystal sizes of approximately 0.25 µm, while the urea-produced powders (Figure 4(b)) are highly agglomerated and with crystals that have coalesced into each other. Thus, the extra heat from the urea combustion promoted sintering through enhanced diffusion.

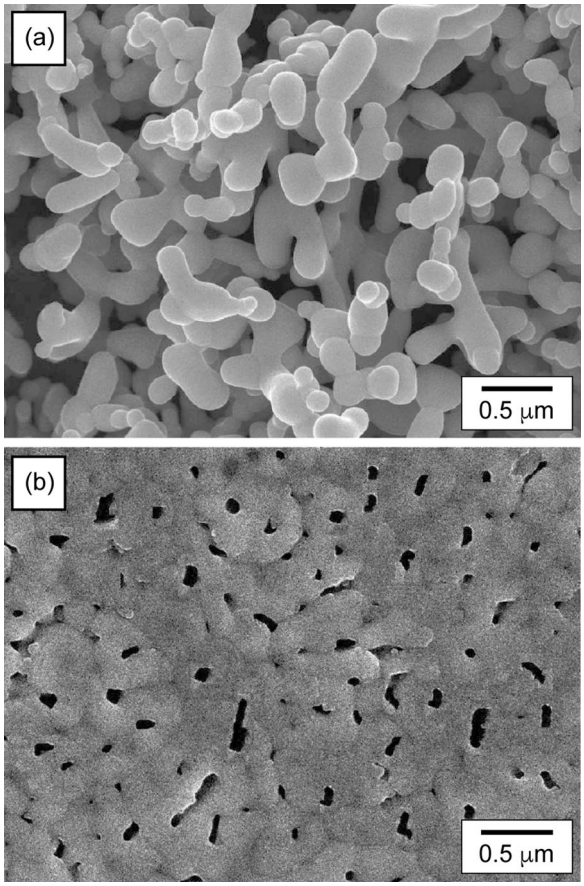

Figure 4. Scanning electron micrographs of Tb-doped $Lu_3Al_5O_{12}$ obtained using (a) glycine and (b) urea. Reprinted with permission [25].

Adiabatic flame temperature

According to [24], the adiabatic flame temperature of the reaction can be estimated by solving

$$\Delta H_{combustion} = \int_{T_o}^{T_{ad}} (\Sigma\ nC_p)_{products} dT, \quad (12)$$

where T_{ad} is the adiabatic flame temperature, T_o is the starting temperature, n is the number of moles of the reaction product, and C_p is the heat capacity of the products at constant pressure. From the enthalpy of formation and heat capacity, this equation can be solved for the theoretical adiabatic flame temperature of the reaction. However, the experimental flame temperature is usually lower than the adiabatic flame temperature because of heat loss during the combustion reaction. Generally, stoichiometric mixtures can approach the adiabatic flame temperature for the system in question. If the mixture is non-stoichiometric (either fuel-rich or fuel-lean) the excess fuel or oxidizer can act as a diluent for the reaction, reducing the temperature achieved by the system. The effect of stoichiometry will be

discussed in more detail in the next section. Because temperature change is extremely fast and high, and because the reaction products can be difficult to predict, the calculation of flame temperature is not straightforward. Solving for the adiabatic flame temperature results in

$$T_{ad} = T_o + \frac{\Delta H^o_{products} - \Delta H^o_{reactants}}{(C_p)_{products}}. \qquad (13)$$

From this expression, there are three options for increasing the flame temperature: (1) increase the enthalpy of formation, $\Delta H^o_{products}$ of the products, (2) reduce the enthalpy of formation, $\Delta H^o_{reactants}$ of the reactants, and (3) reduce the heat capacity of the products. The first option may be achieved by including additives that increase the thermal value of the products. For example, metal powders (particularly aluminium) are commonly used in explosives for this purpose.

Studies have been conducted to observe the effects of various fuels and fuel amounts on the experimental flame temperature. As an example, Purohit et al. [30] determined that the crystallite size of ThO_2 powders grew with an increasing amount of fuel, Lenka et al. [31] demonstrated that combustion reactions for CeO_2 synthesis with glycine reached higher flame temperature leading to larger crystallite sizes, and Lima et al. [32] showed that the adiabatic flame temperature was lower for the synthesis of Cr_2O_3 due to lower amounts of fuel using both glycine and urea, resulting in smaller crystallite sizes.

Earlier, we described the synthesis of Tb-doped $Lu_3Al_5O_{12}$ powders using urea and glycine [25]. For this synthesis, the enthalpy of combustion was lower for the glycine fuel, resulting in smaller crystals. In support of this initial assessment, the flame temperature was found to be lower for reactions with glycine, compared to reactions with urea. Additionally, when increasing the amount of urea in the fuel mix, the corresponding flame temperature increases, and the particle/agglomerate sizes of the resultant materials (estimated from BET) are larger (see Figure 5). Thus, in general, the higher the adiabatic flame temperature, the larger the crystallite size and particle size of

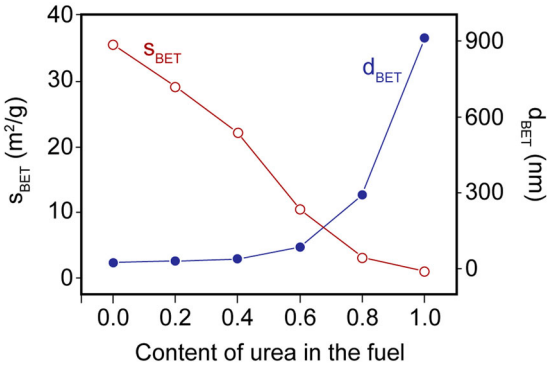

Figure 5. The influence of urea on the surface area and particle size of Tb-doped $Lu_3Al_5O_{12}$. Reprinted with permission [25].

powders. It has also been found that glycine has the highest amount of gases released, thus resulting in the smallest particle sizes for Cr-doped $Y_3Al_5O_{12}$ powders, followed by carbohydrazide and urea [13,33], in support of earlier arguments regarding gas release in these systems.

Figure 6 summarises adiabatic flame temperatures with respect to the enthalpy of formation for typical organic fuels used in combustion synthesis. The reactions produced from citric acid are found to have a dramatically higher adiabatic flame temperature compared to the rest of the fuels, all of which are clustered at the bottom left of the figure. Citric acid also has a much higher enthalpy of formation compared to the rest of the compounds. Thus, the use of this fuel is recommended when higher flame temperatures are desired. Figure 7 summarises crystallite sizes versus adiabatic flame temperature for some of the oxides listed in Table 3. This table may serve as a guide to the reader on expected crystallite sizes for a variety of common oxides prepared using typical fuels. Upon careful analysis, it is seen that the adiabatic flame temperature is not a predictor of the powder crystallite size (Figure 7(a)), as the process has additional complexities that cannot be accounted for by theory. In contrast, the experimental flame temperature (Figure 7(b)) is a better predictor of crystallite size. As flame temperature increases, crystallite size increases for most materials due to thermodynamic particle coarsening effects but the effect is not significant enough to control growth from nanometre to micrometer sizes. That is, powders are nanocrystalline and will not achieve larger sizes

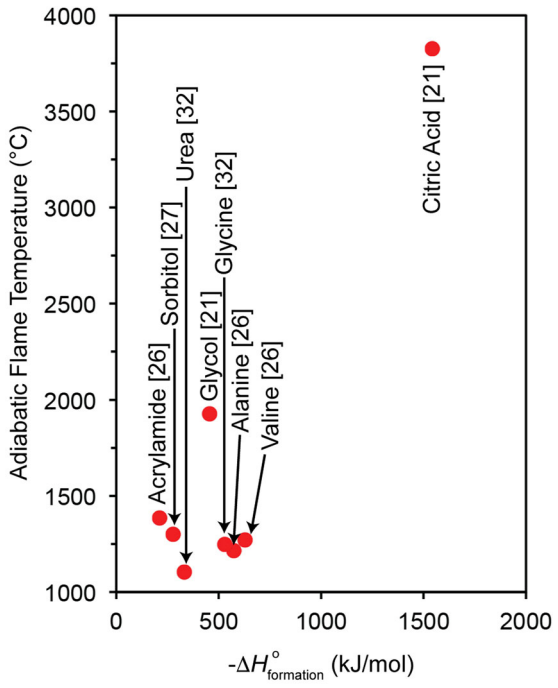

Figure 6. Adiabatic flame temperatures for different organic fuels used for the manufacture of oxide powders by combustion synthesis.

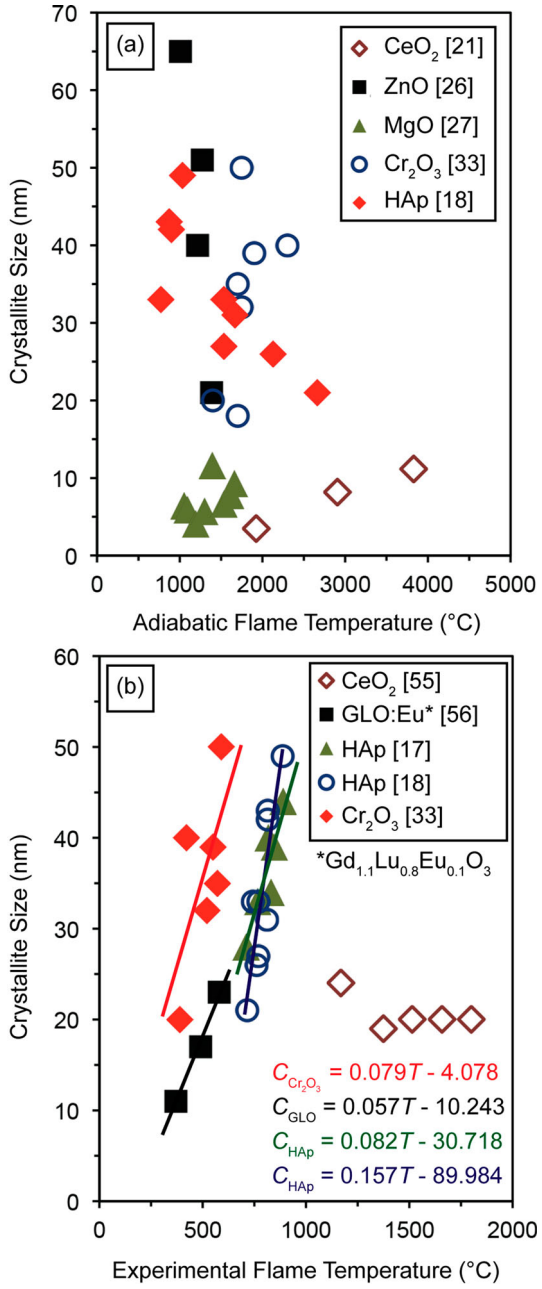

Figure 7. Crystallite sizes versus (a) adiabatic flame temperature and (b) experimental flame temperature for select oxides prepared by combustion synthesis.

because of the extreme shortness of the process. Figure 7(b) illustrates the change in crystallite size with experimental flame temperature for $Gd_{1.1}Lu_{0.8}Eu_{0.1}O_3$ [34], hydroxyapatite [17,18], and Cr_2O_3 [33], describing a linear trend that follows an increase of crystallite size with respect to flame temperature. For example, the Cr_2O_3 powders increase in crystallite size from 20 to 50 nm with an increase in flame temperature from 390°C to 590°C. For the case of the GLO:Eu ($Gd_{1.1}Lu_{0.8}Eu_{0.1}O_3$) powders, there is an increase from 11 to 23 nm with an increase in temperature from 370°C to 580°C. An exception was found for the case of CeO_2 where the crystallite size did not vary with either adiabatic flame temperature or experimental flame temperature [35], showing once again that the process is complex and some appropriate generalities can be made but may not apply to certain materials. In this case, the authors describe a process in which the maximum flame temperature is modified with respect to type of fuel ($T_{\text{aspartic acid}} = 1375°C$, $T_{\text{glutamic acid}} = 1660°C$, $T_{\text{tryptophan}} = 1800°C$, $T_{\text{phenylalanine}} = 1515°C$, $T_{\text{dimethyl urea}} = 1170°C$), resulting in no change in crystallite size ($C_{\text{aspartic acid}} = 19$ nm, $C_{\text{glutamic acid}} = 20$ nm, $C_{\text{tryptophan}} = 20$ nm, $C_{\text{phenylalanine}} = 20$ nm, $C_{\text{dimethyl urea}} = 24$ nm) but some change in particle size ($P_{\text{aspartic acid}} = 11$ μm, $P_{\text{glutamic acid}} = 5$ μm, $P_{\text{tryptophan}} = 8$ μm, $P_{\text{phenylalanine}} = 10$ μm, $P_{\text{dimethyl urea}} = 8$ μm). Thus, changes in the heat of combustion in CeO_2 cause agglomeration of the powders but not crystallite growth. One possible explanation for this effect, albeit unverified from the results presented by Mukherjee et al. [35], may be the presence of unreacted organics that cover the surfaces, preventing crystallite growth, but promoting agglomeration. It is known that combustion synthesis can result in powders with residual organics, especially for fuel-rich mixtures, which is the reason why many powders require a calcination step after synthesis. Thus, the presence of organics in these powders is a possibility.

A summary of particle/agglomerate sizes can be found in Table 4, estimated by transmission electron microscopy (TEM), scanning electron microscopy (SEM), dynamic light scattering (DLS), and the Brunauer–Emmett–Teller (BET) method. DLS [41–59] is by far the most reliable method to measure the particle/agglomerate sizes of powders, and in this contribution, we take special care to differentiate between the crystallite size and particle/agglomerate size.

Fuel-to-oxidizer ratio

The fuel-to-oxidizer ratio is a parameter that controls the combustion temperature and can be estimated according to

$$\phi = \frac{\Sigma(\text{Moles of elements in chemical formula of fuel}) \cdot (\text{valency})}{\Sigma(\text{Moles of elements in chemical formula of oxidizer}) \cdot (\text{valency})}. \quad (14)$$

A specific calculation, described earlier for 1 mol of M $(NO_3)_3$ (M^{3+} = metal ion) and 1 mol of carbohydrazide, results in a ratio of $\phi = 8/15 = 0.53$. One can also calculate a fuel-to-oxidizer equivalence ratio as follows

$$\lambda = \frac{\phi_{\text{test mixture}}}{\phi_{\text{stoichiometric}}} \quad (15)$$

such that $\lambda = 1$ for a stoichiometric test mixture, $\lambda > 1$ for a fuel-rich test mixture, and $\lambda < 1$ for a fuel-lean test mixture. The closer the fuel-to-oxidizer ratio is to stoichiometry (i.e. $\lambda = 1$), the higher the heat of the reaction. Fuel-rich mixtures adversely affect the combustion reaction, providing the conditions suitable

Table 3. Summary of crystallite sizes for different oxide powders prepared using various types of fuels.

Material	Type of fuel	Crystallite size (nm)	Adiabatic flame temperature (°C)	Measured flame temperature (°C)	Reference
α-Al_2O_3	Urea	50[a]	–	–	[36]
	Carbohydrazide	42[a]			
α-Al_2O_3	Urea	98[a]	–	–	[14]
	Sucrose	16[a]			
$Ce_{1-x}Sm_xO$	Citric acid	19.7[a]	–	–	[22]
	Alanine	22.6[a]			
	Glycine	15.6[a]			
CeO_2	Citric acid	11.16[a]	3827	–	[21]
	Glycol	3.48[a]	1927	–	
	Citric acid-glycol	8.18[a]	2910	–	
CeO_2	Aspartic acid	19[a]	–	1375	[35]
	Glutaminic acid	20[a]	–	1660	
	Tryptophan	20[a]	–	1800	
	Phenilalanine	20[a]	–	1515	
	Dimethyl urea	24[a]	–	1170	
Y_2O_3:Bi	Hexamethylenetetramine	29[b]	–	–	[29]
	Glycine	13[b]			
	Urea	9[b]			
$Gd_{1.1}Lu_{0.8}Eu_{0.1}O_3$	Glycine	23[a]	–	580	[34]
	Citric acid	17[a]	–	490	
	Urea	11[a]		370	
$La_{0.7}Sr_{0.3}MnO_3$	Urea	16.0[a]	–	–	[37]
	Glycine	19.6[a]	–	–	
HAp	Stoichiometric Urea	40[a]	–	817	[17]
	Stoichiometric Glycine	44[a]	–	888	
	0.6 Urea + 0.4 Glycine	34[a]	–	830	
	0.4 Urea + 0.6 Glycine	39[a]	–	847	
	Urea + 0.5 g Glucose	33[a]	–	765	
	Urea + 1.0 g Glucose	28[a]	–	709	
HAp	(ϕ = 0.8) Urea	33[a]	769	743	[18]
	(ϕ = 1) Urea	42[a]	896	815	
	(ϕ = 1.5) Urea	31[a]	1670	811	
	(ϕ = 2) Urea	26[a]	2128	760	
	(ϕ = 3) Urea	21[a]	2664	715	
	(ϕ = 0.8) Glycine	43[a]	847	815	
	(ϕ = 1) Glycine	49[a]	1035	887	
	(ϕ = 1.2) Glycine	33[a]	1531	770	
	(ϕ = 1.5) Glycine	27[a]	1531	770	
$LaCrO_3$	Triethanol amine	50.1[a]			[16]
	N-butyl amine	63.3[a]			
	Ethylene diamine	83.8[a]			
$ZnAl_2O_4$	Urea	44[a]			[38]
	Carbohydrazide	48[a]			
	Aniline	40[a]			
$Ce_{0.9}Zr_{0.1}O_2$	Glycine	8.6 ± 4[a]			[39]
	Alanine	8.6 ± 3[a]			
	Lysine	7.9 ± 4[a]			
$Sc_2(WO_4)_3$	Urea	67.2[a]			[40]
	Carbohydrazide	127[a]			
$In_2(WO_4)_3$	Urea	125[a]			[40]
	Carbohydrazide	121[a]			
$MgAl_2O_4$	Urea	3.45[a]			[19]
	Alanine	10.36[a]			
ZnO	Urea	55[b]			[20]
	Glycine	33[b]			
	Citric acid	30[b]			
ZnO	Zinc acetate	65[a]	1008		[27]
	Valine	51[a]	1272		
	Alanine	40[a]	1215		
	Acrylamide	21[a]	1385		
MgO	(ϕ = 0.85) PEG	11.6[a]	1396		[28]
	(ϕ = 1) PEG	9.3[a]	1661		
	(ϕ = 1.15) PEG	7.75[a]	1611		
	(ϕ = 1.4) PEG	6.65[a]	1531		
	(ϕ = 0.85) Sorbitol	6.4[a]	1054		
	(ϕ = 1) Sorbitol	5.7[a]	1301		
	(ϕ = 1.2) Sorbitol	4.1[a]	1192		
	(ϕ = 1.4) Sorbitol	5.9[a]	1090		
Cr_2O_3	4.25 g Urea + 17 g NH_4NO_3	35[a]	1700	570	[33]
	4 g Urea + 31.9 g NH_4NO_3	50[a]	1750	590	
	8.5 g Urea + 34 g NH_4NO_3	20[a]	1400	390	
	3.75 g Glycine	40[a]	2300	420	
	3.75 g Glycine + 18 g NH_4NO_3	32[a]	1750	520	
	7.5 g Glycine + 36 g NH_4NO_3	39[a]	1900	550	
	3.75 g Glycine + 36 g NH_4NO_3	18[a]	1700	390	

[a]X-ray diffraction (XRD).
[b]Transmission electron microscopy (TEM)

Table 4. Summary of particle sizes for different oxide materials prepared using various fuels.

Material	Type of fuel	Particle size (nm)	Method	Reference
α-Al_2O_3	Urea	350	DLS	[36]
	Carbohydrazide	220		
	Urea	250	SEM	
	Carbohydrazide	200		
	Urea	200	TEM	
	Carbohydrazide	150		
α-Al_2O_3	Urea	7220	SEM	[14]
	Sucrose	5660		
$Lu_3Al_5O_{12}$:Tb	Glycine	25–60	SEM	[25]
	Glycine/urea	40–900		
	Urea	900		
$Ce_{1-x}Sm_xO$	Citric acid	24.6	BET	[22]
	Alanine	17.2		
	Glycine	13.0		
CeO_2	Citric acid	22.37	BET	[21]
	Glycol	8.51		
	Citric acid-glycol	19.96		
CeO_2	Aspartic acid	11 µm	BET	[35]
	Glutaminic acid	5 µm		
	Tryptophan	8 µm		
	Phenylalanine	10 µm		
	Dimethyl urea	8 µm		
ZnO	Carbohydrazide	320	SEM	[60]
	Glycine	125		
HAp	Urea	178	BET	[17]
	Glycine	217		
HAp	Urea	180	BET	[18]
	Glycine	216		
$ZnAl_2O_4$	Urea	88.52	BET	[38]
	Carbohydrazide	26.66		
	Aniline	44.17		
	Glycine	49.14		
$Sc_2(WO_4)_3$	Urea	349	DLS	[40]
	Carbohydrazide	711		
$In_2(WO_4)_3$	Urea	219	DLS	[40]
	Carbohydrazide	268		

for premature sintering of powders and corresponding growth of the particles [61]. Figure 8 illustrates the dependence of flame temperature on fuel-to-oxidizer ratio for $(Y_{1-m}Ce_m)_2SiO_5$ [62]. The flame temperature reaches a maximum at fuel-to-oxidizer ratios between 2 and 2.5. This plateau represents a compromise of maximum heat production from the chemical reaction and higher gas release that effectively reduces the flame

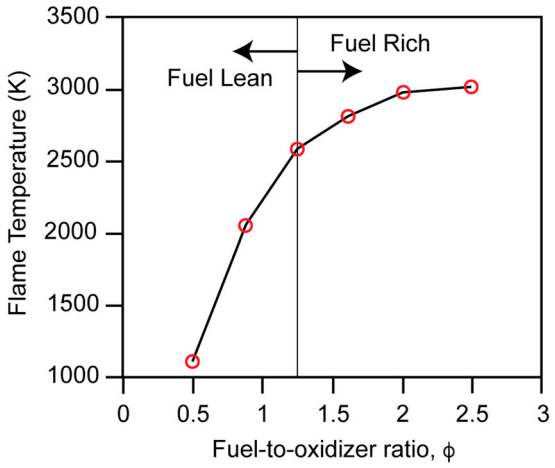

Figure 8. The dependence of adiabatic flame temperature on fuel-to-oxidizer ratio, ϕ, for $(Y_{1-m}Ce_m)_2SiO_5$. Reprinted with permission [62].

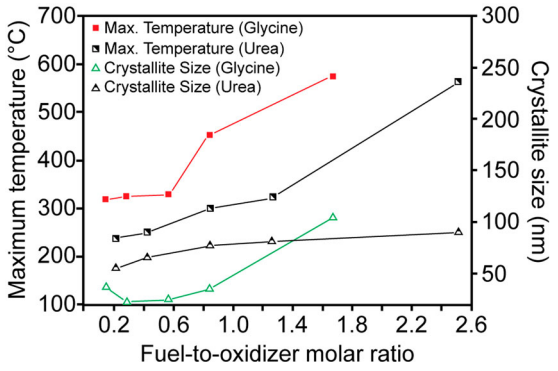

Figure 9. Effect of fuel-to-oxidizer ratio and maximum temperature of combustion for different proportions of glycine-nitrate and urea-nitrate for the synthesis of Co_3O_4 powders by combustion synthesis. Reprinted with permission [63].

temperature. Increasing the amount of fuel further will not increase the flame temperature and will also result in higher amounts of organic residues left on the powders, thus the addition of excessive fuel is not recommended.

Figure 9 illustrates the effect of fuel-to-oxidizer ratio on the crystallite size of Co_3O_4 for two different fuels (glycine and urea). Crystallite sizes increase with an increase in the fuel-to-oxidizer ratio for both fuels. Additionally, the higher the combustion temperature, the larger the crystallite sizes for all fuel-to-oxidizer ratios tested [63]. Ribeiro et al. [64] concluded that the increase of fuel-to-oxidizer ratio not only increases the crystallite size of powders but also changes the distribution of crystallite sizes. In particular, the crystallite sizes of $NiAl_2O_4$ were more uniform for a fuel-to-oxidizer equivalence ratio equal to 1 (stoichiometric conditions), whereas there was a significant size distribution for fuel-to-oxidizer equivalence ratios

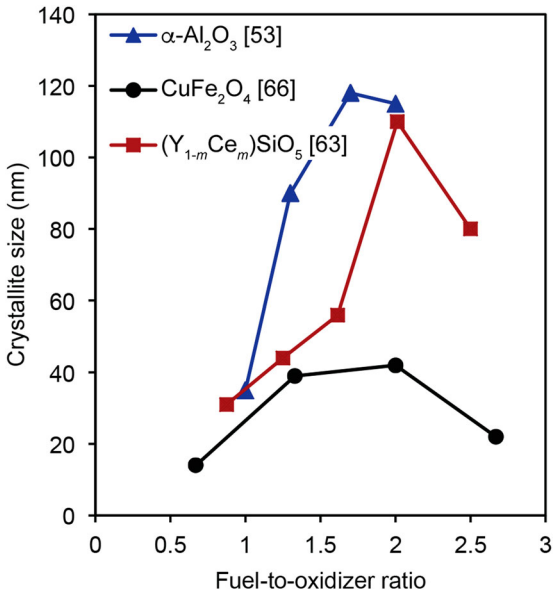

Figure 10. Effect of fuel-to-oxidizer ratio on crystallite sizes of select oxide powders prepared by combustion synthesis.

equal to 1.5 and 2. Figure 10 illustrates representative data for crystallite sizes versus fuel-to-oxidizer ratio for α-Al_2O_3 [36], $CuFe_2O_4$ [65], and $(Y_{1-m}Ce_m)SiO_5$ [65]. An increase of crystallite size up to a certain value of fuel-to-oxidizer ratio (close to 2) can be noted for all materials, after which there is a decrease in crystallite size. For the case of MgO, NiO, and Co_3O_4 [66–68], one also finds a decrease in crystallite size up to the stoichiometric equivalence fuel-to-oxidizer ratio (with values following the trend $d_{\lambda=0.25} = 18$ nm, $d_{\lambda=0.5} = 17$ nm, $d_{\lambda=0.75} = 14$ nm, and $d_{\lambda=1} = 7$ nm, where the heat of combustion is maximum) and subsequent increase in the fuel-rich region ($d_{\lambda=1.25} = 12$ nm, $d_{\lambda=1.5} = 16$ nm, $d_{\lambda=1.75} = 18$ nm, and $d_{\lambda=2} = 16$ nm). As described earlier, crystallite growth is due to the higher flame temperatures achieved in reactions with higher fuel-to-oxidizer ratios, which promotes crystallite growth up to a certain point. The subsequent smaller crystallite sizes may be related to an increasing release of gases that removes heat from the reaction.

Figure 11 illustrates representative TEM images of crystallites for fuel-lean (Figure 11(a)) and stoichiometric fuel-to-oxidizer (Figure 11(b)) ratios for Nd_2O_3 [69]. The size of the powders is clearly larger for the stoichiometric case compared to the fuel-lean one. In addition, Figure 12 demonstrates the change in powder morphology for iron oxide synthesised with different fuel-to-oxidizer ratios. The corresponding morphology changes transition from a cluster of crystallites (Figure 12(a)) for a fuel-to-oxidizer equivalence ratio of 0.1, through thin flakes and sponge-like porous powders for fuel-to-oxidizer equivalence ratios up to 1 (Figure 12(b)–(e)), and to the highly agglomerated morphologies for a fuel-to-oxidizer equivalence ratio of 1.2 (Figure 12(f)), which corresponds to the fuel-rich case. As mentioned earlier, the competition between the heat of the reaction and the amount of released gases is the main reason for these morphology variations [70].

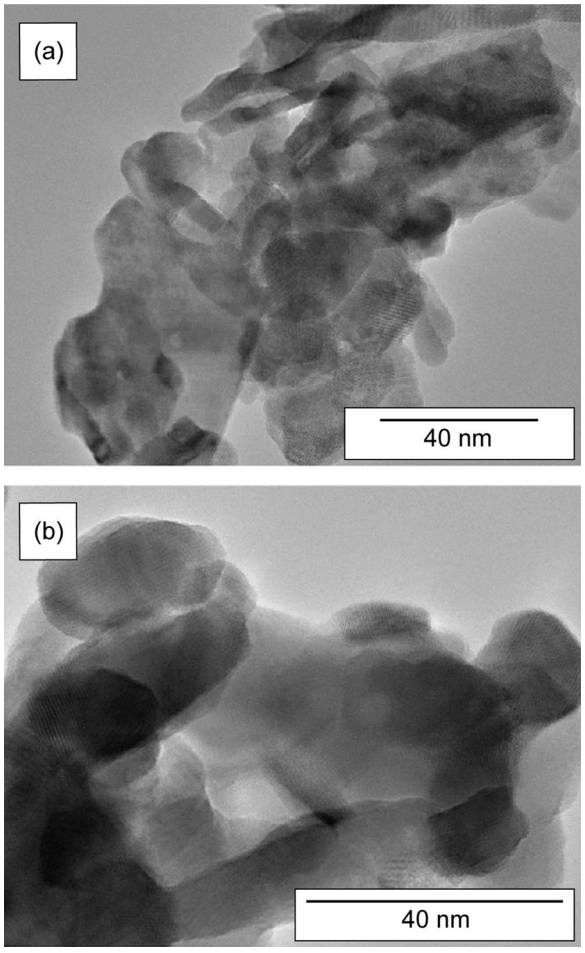

Figure 11. Transmission electron micrographs of (a) Nd_2O_3 powders prepared using a fuel-to-oxidizer ratio that is lean and (b) Nd_2O_3 powders prepared using a stoichiometric fuel-to-oxidizer ratio. Reprinted with permission [69].

The larger amounts of gases produced for reactions with higher fuel-to-oxidizer ratios also affect particle/agglomerate sizes, generally preventing agglomeration. For example, particle sizes of SnO_2 powders measured by BET gas sorption decreased with an increase in fuel-to-oxidizer ratio—in this case citric acid-to-tin ratio [71]. Particle sizes of α-Al_2O_3 measured by DLS were found to increase (416 nm → 679 nm → 887 nm) in fuel-lean reactions, while they decreased (628 nm → 573 nm → 494 nm → 322 nm) in fuel-rich ones because of the large amounts of released gases [72]. A brief summary of crystallite and particle sizes for different fuel-to-oxidizer ratios is presented in Tables 5 and 6, respectively.

Pre-ignition (furnace) temperature

Combustion synthesis reactions take place by placing the reactants in a furnace or hot-plate at mild temperatures. The selection of furnace temperature depends on which fuel is selected, but is typically between about 300°C and 500°C. Below this temperature, there is no ignition. Indeed, at room temperature and atmospheric pressure mixtures such as those in Equations (1), (2) and (4), will not react by themselves. When observing a combustion reaction, nothing seems to occur below the pre-ignition temperature, upon ignition the reaction occurs almost all at once. Figure 13 illustrates a series of images for the combustion synthesis of CaB_6 on a hot-plate using carbohydrazide as fuel. The entire experiment is recorded over an 8 s time frame. The combustion reaction begins at approximately $t = 5$ s and lasts approximately 1–2 s. The kinetics of the process is complex and not completely understood but generally, it can be described by a series of both endothermic and exothermic events, as described in Figure 14. First, an endothermic peak is observed at 76°C due to the melting of the nitrates, followed by a significant endothermic peak at 170°C due to the melting of the carbohydrazide and dehydration, after which detonation and crystallization take place.

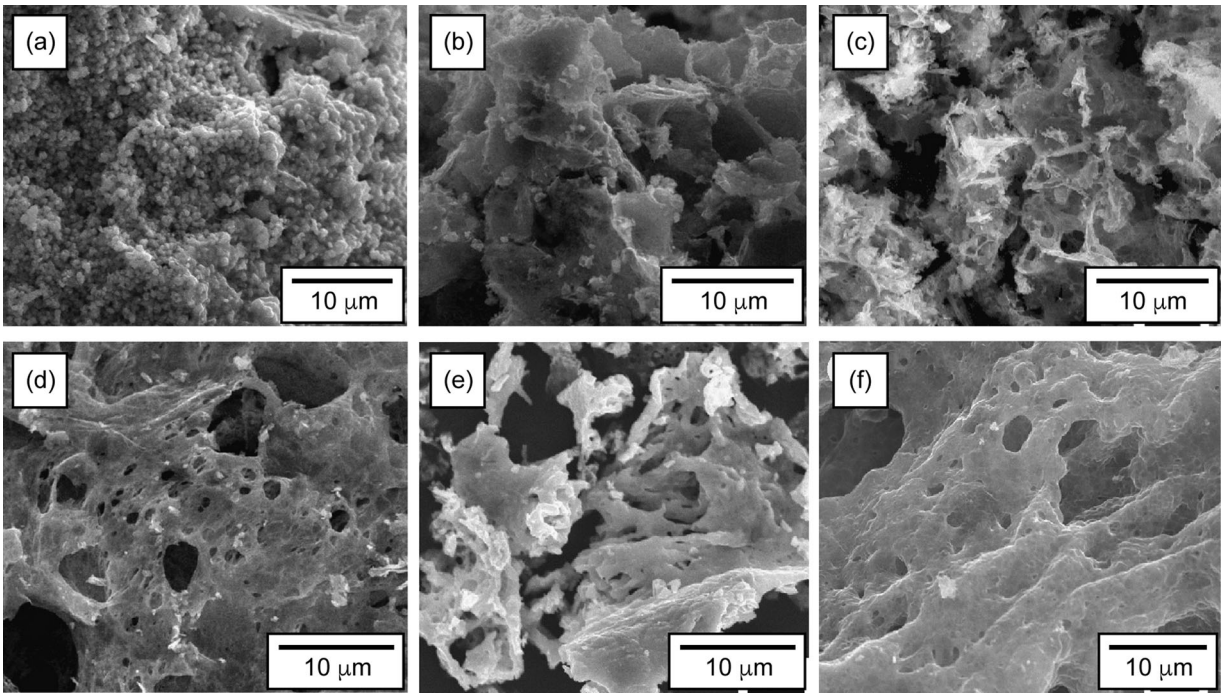

Figure 12. Scanning electron micrographs of iron oxide powders manufactured by combustion synthesis with fuel-to-oxidizer ratios of (a) 0.1, (b) 0.2, (c) 0.3, (d) 0.6, (e) 1, and (f) 1.2. Reprinted with permission [70].

An increasing furnace temperature, above the threshold temperature, adds to the overall system temperature by adding to the heat produced by the exothermicity of the reaction, such that

$$T_{\text{combustion}} = T_{\text{o}} + \frac{\Delta H^{\text{o}}_{\text{products}} - \Delta H^{\text{o}}_{\text{reactants}}}{(C_{\text{p}})_{\text{products}}} + T_{\text{furnace}}. \quad (16)$$

Higher furnace temperature decreases the time for initiation of detonation and improves the crystallinity of the powders, but can also result in a significant increase of particle size. For example, Yang et al. [111] investigated the properties of $LiMn_2O_4$ synthesised at several furnace pre-set temperatures. Depending on temperature, the waiting time for ignition decreased and the particle size became progressively larger, as illustrated in Figure 15(a). $LiMn_2O_4$ exhibits a pronounced linear relationship for all four fuel-to-oxidizer ratios that were tested. On the other hand, crystallite size (Figure 15(b)) also shows an increasing trend with respect to pre-set temperature but the effect varies (and is non-linear) from one material to another. Again here, the complexity of the process and the difficulty in defining fully the reactions taking place, results in variability that cannot be theoretically justified. Crystallite and particle sizes for different furnace pre-set temperatures are listed in Tables 7 and 8.

Additional considerations

Salts

It has been found that there is an increase of the surface area and a decrease of particle and crystallite sizes with the addition of different types of salts [78], since combustion temperature decreases with the addition of the salt (also known as diluent), according to the equation for the enthalpy of combustion with diluents

$$\Delta H_{\text{combustion}} = n_{\text{salt}} \Delta H_{\text{m}} \int_{298}^{T_{\text{ad}}} \sum (nC_{\text{p}})_{\text{products + salt}} \text{d}T, \quad (17)$$

where n_{salt} is the molar amount of added salt, ΔH_{m} is the melting enthalpy of added salt, T_{ad} is the adiabatic flame temperature of the system, and C_{p} is the heat capacity of the products and salt. The adiabatic flame temperature of the reaction without salt is higher than with salt. Therefore, salts attenuate the heat of reaction, lower the temperature of the reaction, and alter the crystallite and particle sizes and the degree of agglomeration of resultant materials. The differences in melting temperatures, solubility, and heat capacity of prospective salts can be tuned to obtain the most optimised properties of the resultant material. Figure 16 illustrates the changes in the sizes and morphologies of the resultant powders for NaCl/metal ratios equal to 0 and 2/3 in $LaMnO_3$ [116]. The addition of NaCl with a simultaneous change in the fuel/oxidizer ratio allows one to produce well-formed small cubic single crystals of

Table 5. Summary of crystallite sizes of oxide materials for different fuels and fuel-to-oxidizer ratios.

Material	Fuel-to-oxidizer ratio	Crystallite size (nm)	Method	Reference
$(Y_{1-m}Ce_m)_2SiO_5$ (carbohydrazide)	0.875	31 (13)	XRD (TEM)	[62]
	1.25	44 (18)		
	1.615	56 (36)		
	2.012	110 (83)		
	2.5	80 (64)		
Lu_2O_3:Eu (glycine)	1	35	XRD	[73]
	1.3	90		
	1.7	118		
	2	115		
Lu_2O_3:Eu (glycine)	0.56	40	XRD	[74]
	0.39	15		
	0.33	5		
	0.28	3		
Y_2O_3:Er (glycine)	1	18	XRD	[75]
	1.2	25		
	1.4	40		
	1.6	50		
	1.8	65		
$BaMgAl_{10}O_{17}:Eu^{2+}$ (urea)	2.36 (stoichiometric)	33	XRD	[76]
	7.08	39		
Y_2O_3:Eu (glycine)	1	8	XRD	[69]
	1.3	40		
	1.7 (stoichiometric)	70		
Nd_2O_3 (glycine)	1	10	XRD	[71]
	1.66	35		
Y_2O_3 (glycine)	0.5	12	XRD	[61]
	1	8		
	1.66	30		
	2	25		
	2.5	9		
	3	9		
CeO_2 (ethylene glycol)	0.75	6.9	XRD	[78]
	1	8.0		
	1.5	14.1		
	2.25	38.2		
Fe_2O_3 (glycine)	0.5	34	XRD	[79]
	1	35		
	2	38		
	4	50		
MgO (PEG)	0.85	11.6	XRD	[28]
	1	9.3		
	1.15	7.75		
	1.4	6.65		
MgO (sorbitol)	0.85	6.4	XRD	[28]
	1.0	5.7		
	1.15	4.1		
	1.4	5.9		
Sc-ZrO_2 (glycine)	0.14	15.9	XRD	[80]
	0.28	11.0		
	0.56	8.2		
	0.84	8.2		
	1.12	7.9		
α-Al_2O_3 (citric acid)	0.033	113	XRD	[72]
	0.1	63		
	0.167	81		
	0.278	64		
	0.333	75		
	0.5	66		
	0.667	74		
MgO (starch)	0.8	5.5	XRD	[81]
	0.9	6.6		
	1.0	7.6		
	1.1	8.3		
CeO_2 (glycine + citric acid)	0.322	44.6	XRD	[82]
	0.377	33.4		
	0.434	20.9		
	0.355	37.9		
	0.410	25.4		
	0.467	11.7		
CeO_2 (glycine)	0.30	10	XRD	[24]
	0.55	15		
	1.00	24		
Co_3O_4 (urea)	0.25	16 ± 0.32	XRD	[66]
	0.5	15 ± 0.3		
	0.75	13 ± 0.26		
	1	6 ± 0.12		
	1.25	11 ± 0.24		

(*Continued*)

Table 5. Continued.

Material	Fuel-to-oxidizer ratio	Crystallite size (nm)	Method	Reference
	1.5	16 ± 0.32		
	1.75	17 ± 0.34		
	2	18 ± 0.36		
MgO (urea)	0.75	30 ± 1.5	XRD	[68]
	1	18 ± 0.9		
	1.25	28 ± 1.4		
	1.5	47 ± 2.4		
	1.75	55 ± 2.8		
	2	53 ± 2.7		
NiO (urea)	0.25	21 ± 0.43	XRD	[67]
	0.5	17 ± 0.34		
	0.75	15 ± 0.30		
	1	7 ± 0.15		
	1.25	21 ± 0.43		
	1.5	32 ± 0.65		
	1.75	38 ± 0.76		
	2	35 ± 0.74		
ZrO_2 (carbohydrazide)	1	5.42	XRD	[83]
	1.25	14.9(t)/8.10(m)		
	1.75	7.60(t)/8.83(m)		
	2.25	6.27(t)/10.60(m)		
Al_2O_3 (glycine)	0.37	90.3	XRD	[84]
	0.43	84.7		
	0.51	90.3		
	0.56	96.8		
	0.69	123.2		
α-Fe_2O_3/Fe_3O_4 (urea)	Stoich	20/22	XRD	[85]
	−50% fuel	35		
	+100% fuel	62/72		
	+200% fuel	54/38		
	+300% fuel	58/36		
	+500% fuel	90/108		
Co_3O_4 (urea)	2.51	90	XRD	[63]
	1.26	81.20		
	0.84	77.00		
	0.42	65.70		
	0.21	55.45		
Co_3O_4 (glycine)	1.67	104.7	XRD	[63]
	0.84	35.00		
	0.56	24.65		
	0.28	22.60		
	0.14	37.10		
SnO_2 (citric acid)	1.4	9.1	XRD	[71]
	2	11.6		
	3	14.2		
	4	18.7		
	6	21.3		
	8	26.7		
CuO (citric acid)	0.28	22.8	XRD	[86]
	0.5	24.5		
	1	27.3		
CuO (urea)	0.625	11.4	XRD	[86]
	0.83	11.4		
	1.25	12.1		
$Mg_{0.2}Fe_{0.8}O$ (glycine)	1	34.4	XRD	[87]
	1.25	27.94		
$NaNbO_3$ (glycine)	0.7	44.51 ± 11.99	XRD	[88]
	0.8	42.59 ± 11.54		
	0.9	37.31 ± 8.54		
	1.0	29.09 ± 5.29		
	1.2	27.45 ± 5.86		
	1.4	26.29 ± 5.97		
	1.6	24.40 ± 4.92		
	1.8	23.79 ± 5.52		
	2.0	26.12 ± 13.69		
$GdFeO_3$ (glycine)	1.1	35	XRD	[89]
	1.2	42		
	1.4	50		
	1.66	65		
$CuFe_2O_4$ (glycine)	0.67	14	XRD	[65]
	1.33	39		
	2.00	42		
	2.67	22		
Hap (urea/glycine)	0.8	33/39	XRD	[18]
	1.5	31/43		
	2	26/33		
	3	21/27		

(*Continued*)

Table 5. Continued.

Material	Fuel-to-oxidizer ratio	Crystallite size (nm)	Method	Reference
$Zr_{0.8}Ce_{0.2}O_2$ (glycine)	1	7	XRD	[90]
	1.22	10		
	1.65	9		
	2	10		
$BiVO_4$ (urea)	3	42	XRD	[91]
	3.5	40		
	4	54		
	4.5	54		
	5	87		
$LiNbO_3$ (glycine)	1	33	XRD	[92]
	2	29		
	3	32		
	4	35		
	5	28		
	6	39		
$MgFe_2O_4$ (glycine)	0.3	37	XRD	[93]
	0.5	33		
	1 (stoichiometric)	28		
	1.5	31		
	2	32		
$LaMnO_{3+\delta}$ (oxalyal dihydrazide)	0.75	32	XRD	[94]
	1.00 (stoichiometric)	36		
	1.25	40		
	1.50	44		
$NiAl_2O_4$ (urea)	1 (stoichiometric)	3.4	XRD	[64]
	1.5	14.2		
	2	16.6		
$CoFe_2O_4$ (glycine)	0.5	33	XRD	[95]
	1 (stoichiometric)	37		
	1.5	38		
$Mn_{0.8}Mg_{0.2}Fe_2O_4$ (urea)	6.67	21.4 ± 0.5	XRD	[96]
	7.7	24.2 ± 0.5		
	9	40.6 ± 0.5		
	10	41.8 ± 0.5		
$Ba(Zr_{0.7}Ce_{0.1}Y_{0.2})O_{2.9}$ (glycine)	0.33	8	XRD	[97]
	0.4	9		
	0.45	11		
	0.5	12		
	0.56	16		
	0.66	17		
	0.75	18		
$Sr_{0.85}Ce_{0.15}FeO_{3-x}$ (citric acid)	1.2	69	XRD	[98]
	2	116		
	4	91		
$La_{0.82}Sr_{0.18}MnO_3$ (glycine)	0.4	13	XRD	[99]
	0.45	17		
	0.5	18.5		
	0.55	19		
	0.6	19		
	0.65	17		
	0.7	12		
$Co_{1-x}Zn_xFe_2O_4$ (glycine)	0.17	6	XRD	[100]
	0.22	10		
	0.28	16		
	0.44	40		
	0.56	46		
	0.66	44		
$Na_3Cr_2(PO_4)_3$ (glycine)	0.33	39.39 ± 4.12	XRD	[101]
	0.5	34.02 ± 2.68		
	1	31.29 ± 3.91		
$Ni_{0.5}Zn_{0.5}Fe_2O_4$ (glycine)	0.25	4	XRD	[102]
	0.5	8		
	1.0	24		
	1.5	45		
Al_2O_3/Y-ZrO_2 (urea)	0.5	10 Al_2O_3/10 Y-ZrO_2	TEM	[103]
	2	44 Al_2O_3/24 Y-ZrO_2	XRD	
	Stoichiometric	60 Al_2O_3/33 Y-ZrO_2	XRD	
CeO_2/Y_2O_3 (glycine)	1–2	4.5-7	XRD	[104]
	2–3	8–18		
Zn/CoO (glycine)	0.2	75	XRD	[105]
	0.4	18		
	0.6	40		
	1	35		
CeO_2/Cu (glycine)	Fuel-rich	Large	XRD	[106]
	Stoichiometric	Large		
	Fuel-lean	Fine		
CeO_2/ZrO_2 (ethylene glycol)	0.5	5.04	XRD	[107]

(*Continued*)

Table 5. Continued.

Material	Fuel-to-oxidizer ratio	Crystallite size (nm)	Method	Reference
	0.62	10.41		
	0.92	16.92		
ZrO_2/MoO_3 (glycine)	0.5	7	XRD	[108]
	0.75	4		
	1	11		
	1.25	15		
	1.5	39		
8YSZ (glycine)	0.756	7.10	XRD	[109]
	0.855	7.05		
	0.940	7.05		
	1.000	7.00		
	1.103	6.80		
	1.163	10.20		
	1.379	13		
	1.605	8.30		

$LaMnO_3$. NaCl behaves as a high-temperature solvent during the combustion reaction resulting in well-dispersed smaller particles. Similar effects have been reported by Tong et al. [117,118] and Zhang et al. [119] for the synthesis of $Er_2Sn_2O_7$, $Er_2Zr_2O_7$, and $CoFe_2O_4$, with additions of KCl. The incorporation of KCl as a reactant minimises agglomeration, as illustrated in Figure 17. Generally, crystallite and particle sizes are greatly reduced with the addition of salts (see Tables 9 and 10). The effects on powders for several different additives are summarised in Table 11.

In regular explosive mixtures used in propellant chemistry applications, the addition of fine metal powders, such as aluminium or magnesium, are used as additives to increase the heat of explosion. For the case of aluminium additions, a partial reaction is

$$2Al + \frac{3}{2}O_2 \longrightarrow Al_2O_3 + 1669\ \text{kJ/mol} \qquad (18)$$

which can also react with explosion products such as CO_2 and H_2O secondarily to obtain

$$2Al + 3CO_2 \longrightarrow Al_2O_3 + 3CO + 593\ \text{kJ/mol}, \qquad (19)$$

$$2Al + 3H_2O \longrightarrow Al_2O_3 + 2H_2 + 944\ \text{kJ/mol}. \qquad (20)$$

From this point of view, combustion synthesis is an extension of the theory of explosive mixtures containing metallic additives and, indeed, the production of nanopowders of Al_2O_3 by this technique is common (see Tables 4, 5, and 7).

Influence of pH

Peng et al. [127] determined the influence of pH (range of 2.5–10.5) for the synthesis of alumina. They concluded that the rate of decomposition, as well as hydrogen bonding between the fuel and metal hydroxides, was responsible for the change in morphology and crystallite sizes of the powders. Unagglomerated particles resulted from a pH value equal to 10.5. Aggregates of nanoparticles were the result of pH equal to 6, and flaky larger particles were the result of pH equal to 2.5. Patra et al. [128] reported similar results for $Ba_{0.5}Sr_{0.5}Co_{0.8}Fe_{0.2}O_3$ prepared using citric acid. Particle sizes estimated from BET were found to be almost three times smaller for the solution of pH 9 compared to those of pH 5. Since citric acid dissociates at higher pH values, it is conjectured that the complexation sites are more readily available to the metal cations, thus more effectively dissolving the nitrates, separating them, and hindering particle growth. On the other hand, Mohebbi et al. [129] investigated the influence of pH of the initial solution (in the range between 0.5 and 9) on the crystallite sizes for the synthesis of Ni/NiO-YSZ composites. It was found that the crystallite sizes became smaller with increasing pH due to faster combustion of the solution.

Modifications of pH during combustion synthesis can also affect other powder properties. For example, the combustion synthesis of HAp at pH values of 4 and 6 resulted in modifications of the stoichiometry of the resulting powders [41,130]. The powders prepared at pH = 4 consisted of calcium-deficient HAp, whereas the powders prepared at pH = 6 consisted of stoichiometric HAp. A schematic representation of the process is illustrated in Figure 18. The change in pH also results in modifications of the particle size. The powders prepared at pH = 4 consist of agglomerates between 160 and 170 nm, whereas the powders prepared at pH = 6 consist of slightly smaller agglomerates between 150 and 167 nm. A brief summary of crystallite and particle sizes for different pH values is provided in Tables 12 and 13.

Challenges, limitations, and recent findings

The combustion synthesis process has been phenomenally successful for the production of a variety of powders, such that online records (publications, abstracts, presentations, etc.) for a 'solution combustion synthesis' search exceeded 28,000 in the year 2019 alone, according to Google Scholar (Figure 19 (a)), for a total of 375,069 records from 1950 to 2019. The same search in INSPEC resulted in a

Table 6. Summary of particle sizes of oxide materials for different fuels and fuel-to-oxidizer ratios.

Material	Fuel-to-oxidizer ratio	Particle size (nm)	Method	Reference
$Lu_3Al_5O_{12}:Tb^{3+}$ (glycine)	1.2	27	BET	[25]
	1.4	35		
	1.5	42		
	1.6	48		
	1.7	60		
α-Al_2O_3 (citric acid)	0.033	416	DLS	[72]
	0.1	679		
	0.167	887		
	0.278	628		
	0.333	573		
	0.5	494		
	0.667	322		
MgO (starch)	0.8	42.4	BET	[81]
	0.9	35.2		
	1.0	27.7		
	1.1	28.6		
CeO_2 (glycine + citric acid)	0.322	65.20	BET	[82]
	0.377	46.39		
	0.434	21.61		
	0.355	63.17		
	0.410	47.97		
	0.467	25.92		
CeO_2 (glycine)	0.30	11	BET	[24]
	0.55	12		
	1.00	22		
Co_3O_4 (urea)	0.25	20 ± 0.6	BET	[66]
	0.5	18 ± 0.54		
	0.75	13 ± 0.39		
	1	8 ± 0.24		
	1.25	13 ± 0.39		
	1.5	17 ± 0.51		
	1.75	18 ± 0.54		
	2	21 ± 0.63		
MgO (urea)	0.75	28 ± 0.56	BET	[68]
	1	12 ± 0.24		
	1.25	29 ± 0.58		
	1.5	46 ± 0.9		
	1.75	62 ± 1.2		
	2	55 ± 1.1		
NiO (urea)	0.25	20 ± 0.5	BET	[67]
	0.5	15 ± 0.4		
	0.75	14 ± 0.36		
	1	7 ± 0.18		
	1.25	22 ± 0.55		
	1.5	35 ± 0.87		
	1.75	39 ± 0.99		
	2	36 ± 0.91		
Al_2O_3 (glycine)	0.2	25.7	BET	[110]
	0.4	30.0		
	0.6	75.2		
	0.8	74.1		
	1.0	29.8		
	1.2	26.0		
SnO_2 (citric acid)	1.4	36.1	BET	[71]
	2	33.8		
	3	31		
	4	28.3		
	6	22.8		
	8	27.8		
MgO (PEG)	0.85	26.4	BET	[28]
	1	19.9		
	1.15	18.2		
	1.4	12.8		
MgO (sorbitol)	0.85	6.4	BET	[28]
	1	5.7		
	1.15	4.1		
	1.4	5.9		
$Mg_{0.2}Fe_{0.8}O$ (glycine)	1	70.9	DLS	[87]
	1.25	70.2		
Hap (urea/glycine)	0.8	140/174	BET	[18]
	1.5	158/212		
	2	132/133		
	3	104/126		
$Sr_{0.85}Ce_{0.15}FeO_{3-x}$(citric acid)	1.2	234	BET	[98]
	2	200		
	4	209		
CeO_2/ZrO_2 (ethylene glycol)	1/2	47.99	BET	[107]
	8/13	49.00		
	12/13	90.10		

total of 3050 publications (Figure 19(b)) from 1950 to 2019, and a total of 2193 in the last decade (Figure 19(c)). While the origins of the technique reside in the study of explosives in the 1950s, its use and recognition for the manufacturing of powders occurred in the 1990s. It is now a workhorse technique in materials science, its success residing in the ease of implementation, high-throughput, the versatility of chemistries, and capacity for the production of high-surface area powders. The main limitations of the technique include problems with powder agglomeration (note Figures 4, 12, and 16), possible lack of control of powder morphologies (note Figure 11), and the presence of leftover carbonaceous and organic impurities from incomplete combustion. Three recent reviews highlight some special topics connected to the technique, including its use for the synthesis of catalytic powders [131] and semiconductors [132], and the utilisation of ecofriendly precursors for the synthesis [133].

Our review focuses primarily on oxides, but combustion synthesis can also be used for the preparation of non-oxide materials. Earlier we mentioned the synthesis of borides [6–10,134], where the relevant combustion reaction is

$$\begin{aligned} \mathrm{La(NO_3)_3} + 6\mathrm{B} + a\mathrm{CH_6N_4O} \longrightarrow \\ \mathrm{LaB_6} + b\mathrm{H_2O} + c\mathrm{CO_2} + d\mathrm{N_2} \\ + \text{ other gases and/or radicals.} \end{aligned} \tag{21}$$

As can be seen, the reaction requires a boron precursor. In this case, the best choice is high-surface area boron metal [6,7], which is mixed into the solution with $La(NO_3)_3$ and carbohydrazide. This example is just one of many that require special choices of precursors that are not nitrates, either because nitrates are not readily available or simply do not exist. Some opportunities include the synthesis of $Sc_2(WO_4)_3$ with ammonium metatungstate hydrate, $(NH_4)_6H_2W_{12}O_{40}\bullet xH_2O$, as the tungsten source [40]; $(Y_{1-m}Ce_m)_2SiO_5$ with fumed SiO_2 as the silicon source [62]; Lu_2SiO_5 with fumed SiO_2 (350–410 m^2/g) as the silicon source [135] $GdV_{0.5}P_{0.5}O_4$ with ammonium metavanadate, NH_4VO_3, as the vanadium source and ammonium phosphate, $NH_4H_2PO_4$, as the phosphorus source [136].

There is also the possibility of producing nitrate, even if it is not available commercially. For example, $(U_{0.5}Ce_{0.5})O_{2\pm x}$ powders were prepared using the

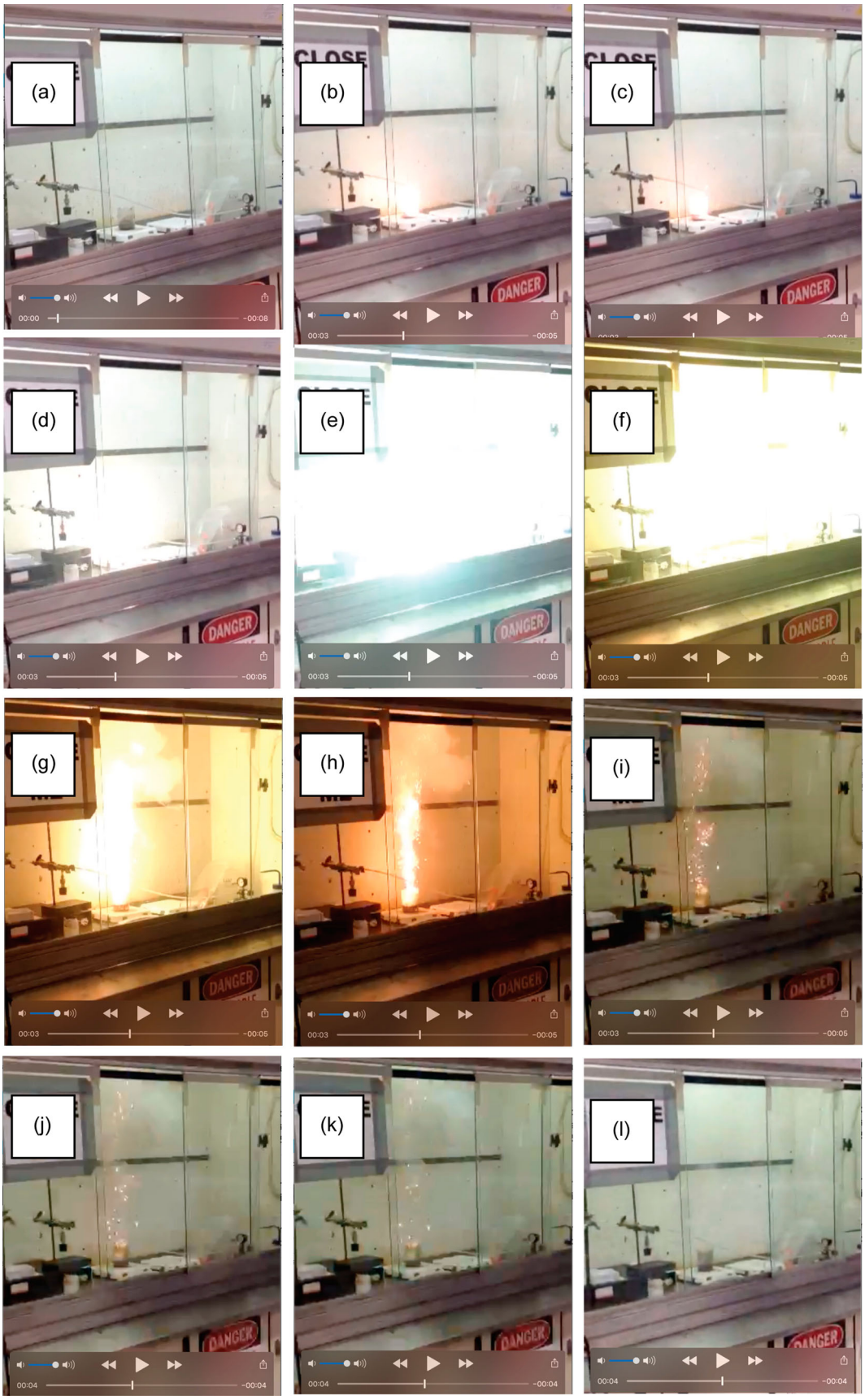

Figure 13. Timed images of the combustion synthesis process for the preparation of CaB_6.

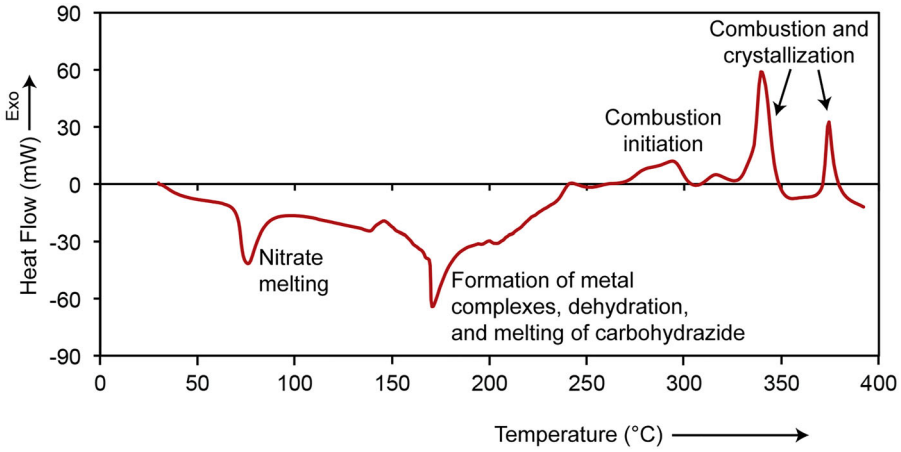

Figure 14. Differential scanning calorimetry of the combustion reaction between lanthanum nitrate, boron, and carbohydrazide. Reprinted with permission [6].

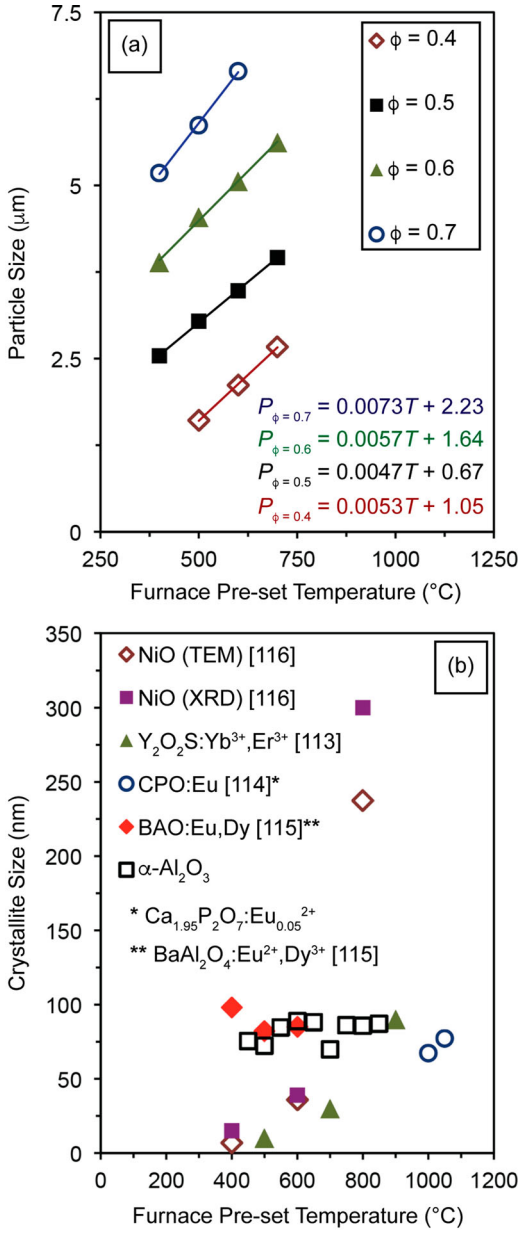

Figure 15. (a) Particle size and (b) crystallite size versus furnace pre-set temperature for a variety of oxide powders prepared by combustion synthesis. For data points provided as ranges of values in Table 7, an average was determined and plotted in (b).

Table 7. Summary of crystallite sizes of oxide materials for different furnace pre-set temperatures.

Material	Furnace temperature (°C)	Crystallite size (nm)	Method	Reference
α-Al_2O_3	450	75.4	XRD	[36]
	500	72.2		
	550	84.5		
	600	88.9		
	650	88.0		
	700	69.8		
	750	86.2		
	800	85.8		
	850	87.1		
NiO	400	~7	TEM	[112]
	600	24–50		
	800	125–350		
	400	15	XRD	
	600	39		
	800	300		
$Y_2O_2S:Yb^{+3},Er^{3+}$	500	10	TEM	[113]
	700	20–40		
	900	70–110		
$Ca_{1.95}P_2O_7:Eu_{0.05}^{2+}$	1000	63.7	XRD	[114]
	1050	77.1		
$BaAl_2O_4:Eu^{2+},Dy^{3+}$	400	98	XRD	[115]
	500	82		
	600	85		

Table 8. Summary of particle sizes of oxide materials for different furnace pre-heat temperatures.

Material	Pre-ignition temperature (°C)	Particle size (μm)	Method	Reference
$LiMn_2O_4$	500	1.61	Centrifugal particle size analyzer	[111]
	600	2.12		
	700	2.67		
	400	2.54		
	500	3.04		
	600	3.48		
	700	3.96		
	400	3.89		
	500	4.54		
	600	5.06		
	700	5.62		
	400	5.18		
	500	5.87		
	600	6.65		
Hydroxyapatite	300	0.164	BET	[18]
	400	0.171		
	500	0.184		
	600	0.216		
	650	0.233		
	700	0.240		

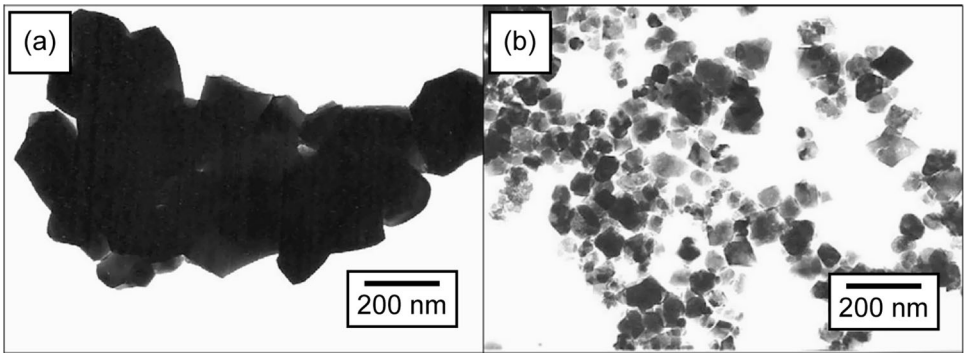

Figure 16. Transmission electron micrographs of $LaMnO_3$ powders prepared by combustion synthesis with (a) NaCl/metal ions = 0 and (b) NaCl/metal ions = 2/3 ratios. Reprinted with permission [116].

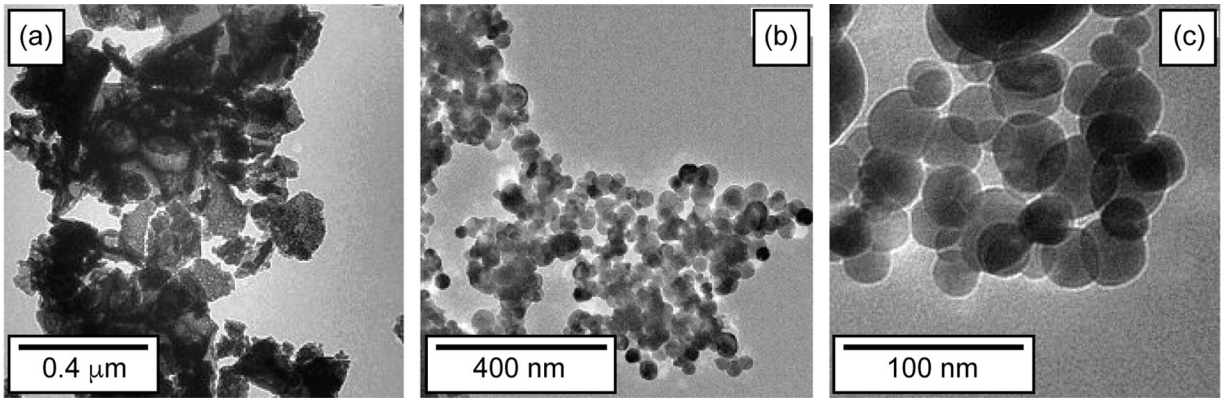

Figure 17. Transmission electron micrographs of $Er_2Zr_2O_7$ powders prepared by combustion synthesis (a) in the absence of KCl and (b)-(c) in the presence of KCl. Reprinted with permission [118].

following combustion reaction [137]

$$UO_2(NO_3)_2 + Ce(NO_3)_3 + aC_6H_8O_7 \longrightarrow 2(U_{0.5}Ce_{0.5})O_{2+x} + bH_2O + cCO_2 + dN_2 + \text{other gases.} \quad (22)$$

However, $UO_2(NO_3)_2$ is not a commercial product. Instead, it was synthesised from commercial U_3O_8 powders that were reacted with nitric acid.

Another possibility is the existence of a highly unstable metal nitrate, which may even be available commercially on a limited basis. For example, titanium (IV) nitrate is a volatile compound that readily sublimes and it is not easy to work with in a laboratory setting. Instead, researchers have developed a variety of options for the use of other compounds during combustion synthesis. For example, for the preparation of titanate compounds such as $CaTiO_3$ [138], the titanium source used

Table 9. Crystallite sizes of various oxide materials with salt additives added as a diluent.

Material	Additive	Crystallite size (nm)	Method	Reference
CeO_2	Without additive	14.10	XRD	[78]
	NaCl	7.04		
	KCl	5.34		
	$CaCl_2$	6.84		
	KCl/LiCl	6.41		
	KCl/$CaCl_2$	5.31		
$CoFe_2O_4$	without KCl	42	XRD	[119]
	with KCl	20		
$CdSiO_3:Co^{2+}$	NH_4F, NaCl, NH_4Cl	50–140	XRD	[120]
$Y_2SiO_5:Sm^{3+}$	Without flux	14	XRD	[121]
	NaCl-flux	41		
	KI-flux	32		
	NH_4Br-flux	32		
	NH_4Cl-flux	20		
	NH_4F-flux	16		

Table 10. Particle sizes of various oxide materials with salt additives added as a diluent.

Material	Additive	Particle size	Method	Reference
$BaMgAl_{10}O_{17}:Eu^{2+}$	PEG	10-50 nm	DLS	[122]
α-Al_2O_3	NH_4NO_3 (urea)	200 nm	DLS	[36]
	NaN_3 (urea)	200 nm		
	NH_4Cl (urea)	150 nm		
	NH_4NO_3 (CH)	150 nm		
	NaN_3 (CH)	175 nm		
	NH_4Cl (CH)	100 nm		
CeO_2	Without additive	59.68 nm	BET	[78]
	NaCl	7.51 nm		
	KCl	5.37 nm		
	$CaCl_2$	10.44 nm		
	KCl/LiCl	9.83 nm		
	KCl/$CaCl_2$	5.59 nm		
$LaMnO_3$	NaCl/Metal = 0	200 nm	TEM	[116]
	NaCl/Metal = 2/3	50-180 nm		
Mullite	NH_4NO_3 (100%)	82 μm	BET	[123]
	HNO_3 (100%)	61 μm		
	NH_4Cl (100%)	71 μm		
	H_2O_2 (100%)	123 μm		
	NH_4NO_3 (200%)	83 μm		
	HNO_3 (200)	85 μm		
	NH_4Cl (200%)	141 μm		
	H_2O_2 (200%)	168 μm		

Table 11. Effect of additives on the combustion reaction and morphology of oxide materials.

Material	Additive	Effects	Reference
Binary oxides	KCl	Increases the surface area	[78]
	NaCl	Reduces crystallite and particle sizes	
	$CaCl_2$	Reduces the degree of agglomeration of crystallites/particles	
	Al_2O_3	Decreases the combustion temperature	[36]
	NH_4NO_3,	Reduces particle size	
	NH_4Cl,	Increases gas release from the system	
	NaN_3	Reduces particle size	
Ternary oxides	KCl	Reduces the size and degree of agglomeration of crystallites/particles	[118]
		Accelerates mass transfer	
	NaCl	Reduces the size and degree of agglomeration of crystallites/particles	[116]
		Accelerates combustion reaction	
	NH_4NO_3	Reduces the size and degree of agglomeration of crystallites/particles	[124]
Composites	NH_4NO_3	Behaves as an oxidant	[123]
		Increases the surface area	[103]
		Works as a combustion aid promoting phase formation without an additional calcination step	
		Increases the surface area	
	NaCl	Reduces crystallite/particle sizes	[78]
Luminescent materials	H_3BO_3	Promotes the formation of additional phases	[125]
		Increases luminescence response	
	LiCl, LiF	Slightly increases the crystallite size	[126]
	Li_2SO_4	Changes the particle morphology	
	NH_4F	Increases crystallinity	
	NH_4Cl	Increases crystallinity	[120]
	NaCl		

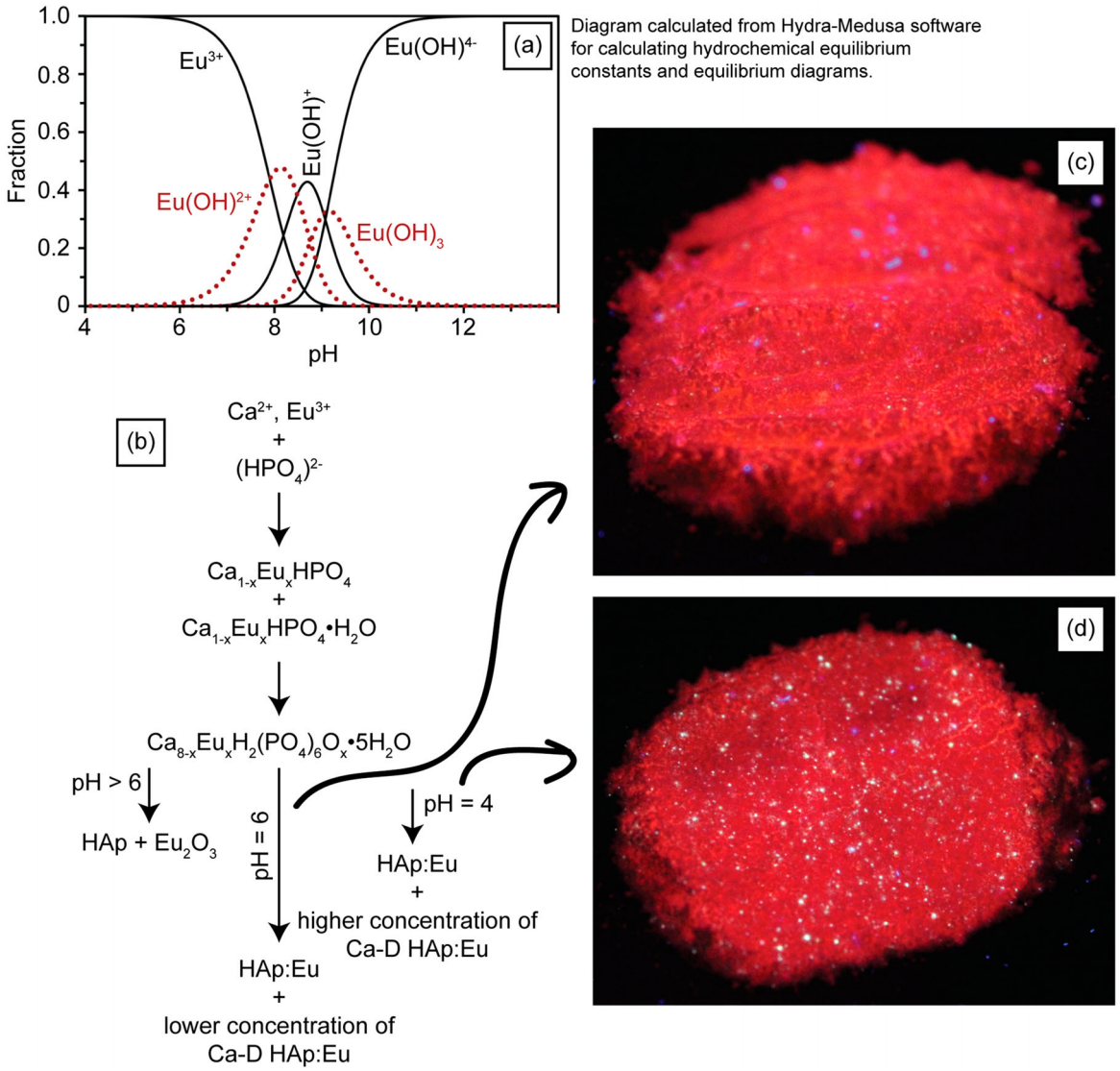

Figure 18. (a) Speciation diagram of Eu simulated with Hydra-Medusa software and (b) formation mechanism of Eu^{2+} in HAp and calcium-deficient HAp powders. Luminescence images of the powders prepared at (c) pH = 6 and (d) pH = 4, generated by UV irradiation revealing the emission of red and blue light, respectively. Reprinted with permission [41].

Table 12. Effect of pH on crystallite sizes of oxide materials.

Material	pH value	Crystallite size (nm)	Method	Reference
α-Al_2O_3	2.5	9.6	XRD	[127]
	6	16.9		
	10.5	19.8		
YSZ-(NiO/Ni)	0.5	32–(33/33)	XRD	[129]
	3	28–(28/28)		
	5	24–(17/23)		
	9	13–(8/15)		

Table 13. Effect of pH on particle sizes of oxide materials.

Material	pH	Particle size (nm)	Method	Reference
$Ba_{0.5}Sr_{0.5}Co_{0.8}Fe_{0.2}O_3$	5	149	BET	[128]
	7	86		
	9	56		
HAp:Eu	4	160–170	DLS	[41]
	6	150–167		

was titanium peroxo citrate, which was produced from reacting TiO, H_2O_2, NH_3, and citric acid. For the synthesis of $In_{14}TiO_{23}$, the titanium source was titanium (IV) isopropoxide [139]. In general, metallorganics can be used in combustion synthesis reactions, as long as they do not hinder the combustion reaction by decreasing the exothermic heat of reaction.

Compounds containing carbon are also possible. The synthesis of CNTs/C/$NiMoO_4$ composites is possible by reacting [140]

$$7Ni(NO_3)_2 + (NH_4)_6Mo_7O_{24} + aC_6H_8O_7 + xCNTs \longrightarrow 7NiMoO_4 + bCO_2 + cN_2 + dH_2O + yCNTs + \text{other gases}, \quad (23)$$

where CNTs (carbon nanotubes) are mixed directly into the reactants. While there is a definite expectation that some of the nanotubes will decompose and form graphite, some will not decompose, resulting in a composite that contains a mixture of CNTs and carbon, as well as the $NiMoO_4$. Note in this case that the molybdenum also requires a special (non-nitrate) precursor.

A final and interesting example corresponds to reactions for the formation of sulphides. Powders of α-NiS, NiS_2, Ni_3S_2 can be produced by reacting Ni $(NO_3)_2$•$6H_2O$, $CS(NH_2)_2$ (thiourea), and urea or glycine as fuel [141,142], whereas powders of ZnS can be produced by reacting $Zn(NO_3)_2$•$6H_2O$ and thiourea, which serves both as the source of sulphur and as the fuel [143].

Summary

We describe the characteristics of powders prepared by the technique of combustion synthesis. A controlling parameter is the fuel-to-oxidizer ratio, ϕ. With all else constant, ϕ determines the energy released and therefore reaction temperature achieved during combustion. A theoretically maximum temperature

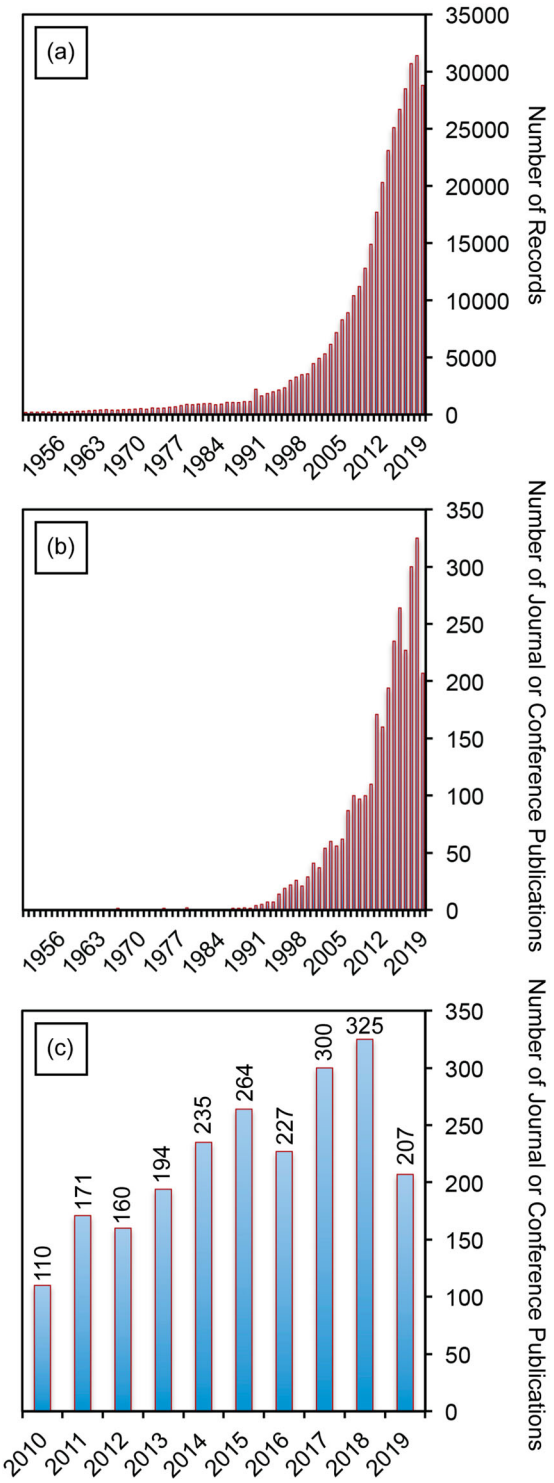

Figure 19. Number of publications in the area of 'solution combustion synthesis' from (a) Google Scholar (excluding patents) from 1950 to 2019, (b) INSPEC from 1950 to 2019, and (c) INSPEC from 2010 to 2019.

is reached when ϕ is stoichiometric and the precursors completely react to form solid and gaseous products. The combustion temperature is systematically lowered as the mixtures become fuel-lean because of the diluting effect of excess oxidizer precursors and can be used to control crystal nucleation and growth. The majority of gaseous products are produced from burning fuel and so greater quantities of gases are produced for fuel-rich mixtures. Thus, fuel-rich

compositions favour the production of larger quantities of gas that result in smaller crystallite sizes. Greater amounts of impurities also result from increasingly fuel-rich compositions due to incomplete burning of the fuel. Other important parameters include the pre-ignition temperature and the addition of salts and diluent precursors to the reactants.

Acknowledgements

This work was supported by grant 1911372 from the National Science Foundation. Support in data verification from T. Ren, A. Yazdani, S. Choi, C.I. Vargas-Consuelos, R. Ridley, M. Sanchez, F.M. Martinez-Pallares, and Hamed Hosseini-Toudeshki, is gratefully acknowledged.

Disclosure statement

No potential conflict of interest was reported by the author(s).

Funding

This work was supported by National Science Foundation [grant number 1911372].

ORCID

Sarit Bhaduri http://orcid.org/0000-0002-5961-7553
Olivia A. Graeve http://orcid.org/0000-0003-3599-0502

References

[1] Shea LE, McKittrick J, Lopez OA, et al. Advantages of self-propagating combustion reactions for synthesis of oxide phosphors. J Soc Inf Disp. 1997;5:117–125.
[2] Mukasyan AS, Dinka P. Novel approaches to solution–combustion synthesis of nanomaterials. Int J Self Propag High Temp Synth. 2007;16:23–35.
[3] Patil KC, Aruna ST, Mimani T. Combustion synthesis: an update. Curr Opin Solid State Mater Sci. 2002;6:507–512.
[4] Tyagi AK, Chavan SV, Purohit RD. Visit to the fascinating world of nano-ceramic powders via solution-combustion. Indian J Pure Appl Phys. 2006;44:113–118.
[5] Tyagi AK. Combustion synthesis: a soft-chemical route for functional nano-ceramics. BARC Newsl. 2007;285:39–48.
[6] Kanakala R, Rojas-George G, Graeve OA. Unique preparation of hexaboride nanocubes: a first example of boride formation by combustion synthesis. J Am Ceram Soc. 2010;93:3136–3141.
[7] Kanakala R, Escudero R, Rojas-George G, et al. Mechanisms of combustion synthesis and magnetic response of high-surface-area hexaboride compounds. ACS App Mater Interfaces. 2011;3:1093–1100.
[8] Cahill JT, Vasquez VR, Misture ST, et al. Effect of current on diffusivity in metal hexaborides. ACS Appl Mater Interfaces. 2017;9:37357–37363.
[9] Cahill JT, Alberga M, Bahena J, et al. Phase stability of mixed-cation alkaline-earth hexaborides. Cryst Growth Des. 2017;17:3450–3461.
[10] Kelly JP, Kanakala R, Graeve OA. A solvothermal approach for the preparation of nanostructured carbide and boride ultra-high temperature ceramics. J Am Ceram Soc. 2010;93:3035–3038.
[11] Sharma P, Lotey GS, Singh S, et al. Solution-combustion: the versatile route to synthesize silver nanoparticles. J Nanopart Res. 2011;13:2553–2561.
[12] Zhu J, Xiao D, Li J, et al. Characterization of $FeNi_3$ alloy in Fe–Ni–O system synthesized by citric acid combustion method. Scr Mater. 2006;54:109–113.
[13] Shea LE, McKittrick J, Lopez OA, et al. Synthesis of red-emitting, small particle size luminescent oxides using an optimized combustion process. J Am Ceram Soc. 1996;79:3257–3265.
[14] Ganesh I, Torres PMC, Ferreira JMF. Densification ability of combustion-derived Al_2O_3 powders. Ceram Int. 2009;35:1173–1179.
[15] Rashad MM, El-Sheikh SM. Magnetic properties of nano-clusters lanthanum chromite powders doped with samarium and strontium ions synthesized via a novel combustion method. Mater Res Bull. 2011;46:469–477.
[16] Lakshmi VV, Bauri R, Paul S. Effect of fuel type on microstructure and electrical property of combustion synthesized nanocrystalline scandia stabilized zirconia. Mater Chem Phys. 2011;126:741–746.
[17] Ghosh SK, Prakash A, Datta S, et al. Effect of fuel characteristics on synthesis of calcium hydroxyapatite by solution combustion route. Bull Mater Sci. 2010;33:7–16.
[18] Ghosh SK, Roy SK, Kundu B, et al. Synthesis of nano-sized hydroxyapatite powders through solution combustion route under different reaction conditions. Mater Sci Eng: B. 2011;176:14–21.
[19] Pacurariu C, Lazau I, Ecsedi Z, et al. New synthesis methods of $MgAl_2O_4$ spinel. J Eur Ceram Soc. 2007;27:707–710.
[20] Deorsola FA, Vallauri D. Synthesis of ZnO nanoparticles through the impregnated layer combustion synthesis process. J Mater Sci. 2011;46:781–786.
[21] Gu L, Meng G. Powder synthesis and characterization of nanocrystalline CeO_2 via the combustion processes. Mater Res Bull. 2007;42:1323–1331.
[22] Chung DY, Lee EH. Microwave-induced combustion synthesis of Ce1−xSmxO2−x/2 powder and its characterization. J Alloy Compd. 2004;374:69–73.
[23] Lopez OA, McKittrick JM, Shea LE. Fluorescence properties of polycrystalline Tm^{3+} activated $Y_3Al_5O_{12}$ and Tm^{3+}-Li^+ co-activated $Y_3Al_5O_{12}$ in the visible and near IR ranges. J Lumin. 1997;71:1–11.
[24] Purohit RD, Sharma BP, Pillai KT, et al. Ultrafine ceria powders via glycine-nitrate combustion. Mater Res Bull. 2001;36:2711–2721.
[25] Liao Y, Jiang D, Feng T, et al. Fabrication, structural, and spectroscopic investigation of Tb-doped $Lu_3Al_5O_{12}$ phosphor. J Mater Res. 2005;20:2934–2939.
[26] Dorofeeva OV, Ryzhnova ON. Revision of standard molar enthalpies of formation of glycine and L-alanine in the gaseous phase on the basis of theoretical calculations. J Chem Thermodyn. 2009;41:433–438.

[27] Ianos R, Lazau I, Pacurariu C, et al. Aqueous combustion synthesis and characterization of ZnO powders. Mater Chem Phys. 2011;129:881–886.
[28] Esmaeili E, Khodadadi A, Mortazavi Y. Microwave-induced combustion process variables for MgO nanoparticle synthesis using polyethylene glycol and sorbitol. J Eur Ceram Soc. 2009;29:1061–1068.
[29] [cited 2020 April 24]. https://en.wikipedia.org/wiki/Hexamethylenediamine.
[30] Purohit RD, Saha S, Tyagi AK. Nanocrystalline thoria powders via glycine-nitrate combustion. J Nucl Mater. 2001;288:7–10.
[31] Lenka RK, Mahata T, Sinha RK, et al. Combustion synthesis of gadolinia-doped ceria using glycine and urea fuels. J Alloy Compd. 2008;466:326–329.
[32] Lima MD, Bonadimann R, de Andrade MJ, et al. Nanocrystalline Cr_2O_3 and amorphous CrO_3 produced by solution combustion synthesis. J Eur Ceram Soc. 2006;26:1213–1220.
[33] McKittrick J, Bacalski CF, Shea LE, et al. The influence of processing parameters on luminescent oxides produced by combustion synthesis. Displays. 1999;19:169–172.
[34] Wu YT, Qin LS, Shi HS, et al. Preparation of europium-doped gadolinium lutetium oxide solid solution transparent ceramics and its optical properties. IEEE Trans Nucl Sci. 2010;57:1343–1347.
[35] Mukherjee ST, Bedekar V, Patra A, et al. Study of agglomeration behavior of combustion-synthesized nano-crystalline ceria using new fuels. J Alloy Compd. 2008;466:493–497.
[36] Chen CC, Huang KT. Parametric effects of low-temperature combustion synthesis of alumina. J Mater Res. 2005;20:424–431.
[37] Conceicao L, Ribeiro NFP, Furtado JGM, et al. Effect of propellant on the combustion synthesized Sr-doped $LaMnO_3$ powders. Ceram Int. 2009;35:1683–1687.
[38] Viana KMS, Dantas BB, Nogueira NAS, et al. Influence of fuel in the $ZnAl_2O_4$ catalytic supports by combustion reaction. Mater Sci Forum. 2010;660-661:52–57.
[39] Zimicz MG, Fábregas IO, Lamas DG, et al. Effect of synthesis conditions on the nanopowder properties of $Ce_{0.9}Zr_{0.1}O_2$. Mater Res Bull. 2011;46:850–857.
[40] Higgins BB, Graeve OA, Edwards DD. New methods for preparing submicrometer powders of the tungstate-ion conductor $Sc_2(WO_4)_3$ and its Al and In analogs. J Am Ceram Soc. 2013;96:2402–2410.
[41] Zavala-Sanchez LA, Hirata GA, Novitskaya E, et al. Distribution of Eu^{2+} and Eu^{3+} ions in hydroxyapatite: a cathodoluminescence and Raman study. ACS Biomater Sci Eng. 2015;1:1306–1313.
[42] Graeve OA, Kanakala R, Madadi A, et al. Luminescence variations in hydroxyapatites doped with Eu^{2+} and Eu^{3+} ions. Biomaterials. 2010;31:4259–4267.
[43] Sinha K, Pearson B, Casolco SR, et al. Synthesis and consolidation of $BaAl_2Si_2O_8$:Eu: development of an integrated process for luminescent smart ceramic materials. J Am Ceram Soc. 2009;92:2504–2511.
[44] Graeve OA, Varma S, Rojas-George G, et al. Synthesis and characterization of luminescent yttrium oxide doped with Tm and Yb. J Am Ceram Soc. 2006;89:926–931.
[45] Graeve OA, Sinha K. Dynamic light scattering study of reverse micellar systems for the synthesis of iron-based nanofluids. Int J Mod Phys B. 2007;21:4774–4781.
[46] Sinha K, Kavlicoglu B, Liu Y, et al. A comparative study of thermal behavior of iron and copper nanofluids. J Appl Phys. 2009;106:064307.
[47] Graeve OA, Madadi A, Kanakala R, et al. Analysis of particle and crystallite size in tungsten nanopowder synthesis. Metall Mater Trans A. 2010;41:2691–2697.
[48] Vasquez VR, Williams BC, Graeve OA. Stability and comparative analysis of AOT/water/isooctane reverse micelles system using dynamic light scattering and molecular dynamics. J Phys Chem B. 2011;115:2979–2987.
[49] Saterlie MS, Sahin H, Kavlicoglu B, et al. Particle size effects in the thermal conductivity enhancement of copper-based nanofluids. Nanoscale Res Lett. 2011;6:217.
[50] Saterlie MS, Sahin H, Kavlicoglu B, et al. Surfactant effects on dispersion characteristics of copper-based nanofluids: a dynamic light scattering study. Chem Mater. 2012;24:3299–3306.
[51] Graeve OA, Fathi H, Kelly JP, et al. Reverse micelle synthesis of oxide nanopowders: mechanisms of precipitate formation and agglomeration effects. J Colloid Interface Sci. 2013;407:302–309.
[52] Vargas-Consuelos CI, Seo K, Camacho-Lopez M, et al. Correlation between particle size and Raman vibrations in WO_3 powders. J Phys Chem C. 2014;118:9531–9537.
[53] Cahill JT, Ruppert JN, Wallis B, et al. Development of mesoporosity in scandia-stabilized zirconia: particle size, solvent, and calcination effects. Langmuir. 2014;30:5585–5591.
[54] Frank MB, Naleway SE, Haroush T, et al. Stiff, porous scaffolds from magnetized alumina particles aligned by magnetic freeze casting. Mater Sci Eng C. 2017;77:484–492.
[55] Frank MB, Siu SH, Karandikar K, et al. Synergistic structures from magnetic freeze casting with surface magnetized alumina particles and platelets. J Mech Behav Biomed Mater. 2017;76:153–163.
[56] Seo K, Sinha K, Novitskaya E, et al. Polyvinylpyrrolidone (PVP) effects on iron oxide nanoparticle formation. Mater Lett. 2018;215:203–206.
[57] Ren T, Nforbi LNN, Kanakala R, et al. Phase stability and mechanisms of transformation of La-doped γ-alumina. Inorg Chem. 2018;57:3035–3041.
[58] Fathi H, Kelly JP, Vasquez VR, et al. Ionic concentration effects on reverse micelle size and stability: implications for the synthesis of nanoparticles. Langmuir. 2012;28:9267–9274.
[59] Kelly JP, Graeve OA. Statistical experimental design approach for the solvothermal synthesis of nanostructured tantalum carbide powders. J Am Ceram Soc. 2011;94:1706–1715.
[60] Park S, Yoo K, Park HJ, et al. Rapid gold ion recovery from wastewater by photocatalytic ZnO nanopowders. J Electroceramics. 2006;17:831–834.
[61] Chavan SV, Pillai KT, Tyagi AK. Combustion synthesis of nanocrystalline yttria: tailoring of powder properties. Mater Sci Eng B. 2006;132:266–271.
[62] Bosze EJ, McKittrick J, Hirata GA. Investigation of the physical properties of a blue-emitting phosphor

produced using a rapid exothermic reaction. Mater Sci Eng B. 2003;B97:265–274.
[63] Toniolo JC, Takimi AS, Bergmann CP. Nanostructured cobalt oxides (Co_3O_4 and CoO) and metallic Co powders synthesized by the solution combustion method. Mater Res Bull. 2010;45:672–676.
[64] Ribeiro NFP, Neto RCR, Moya SF, et al. Synthesis of $NiAl_2O_4$ with high surface area as precursor of Ni nanoparticles for hydrogen production. Int J Hydrogen Energy. 2010;35:11725–11732.
[65] Deraz NM. Size and crystallinity-dependent magnetic properties of copper ferrite nano-particles. J Alloys Compd. 2010;501:317–325.
[66] Rao KV, Sunandana CS. Co_3O_4 nanoparticles by chemical combustion: effect of fuel to oxidizer ratio on structure, microstructure and EPR. Solid State Commun. 2008;148:32–37.
[67] Rao KV, Sunandana CS. Effect of fuel to oxidizer ratio on the structure, micro structure, and EPR of combustion synthesized NiO nanoparticles. J Nanosci Nanotechnol. 2008;8:4247–4253.
[68] Rao KV, Sunandana CS. Structure and microstructure of combustion synthesized MgO nanoparticles and nanocrystalline MgO thin films synthesized by solution growth route. J Mater Sci. 2008;43:146–154.
[69] Chavan SV, Sastry PUM, Tyagi AK. Combustion synthesis of nano-crystalline Nd-doped ceria and Nd_2O_3 and their fractal behavior as studied by small angle X-ray scattering. J Alloys Compd. 2008;456:51–56.
[70] Cao Z, Qin M, Jia B, et al. One pot solution combustion synthesis of highly mesoporous hematite for photocatalysis. Ceram Int. 2015;41:2806–2812.
[71] Zhang J, Gao L. Synthesis of antimony-doped tin oxide (ATO) nanoparticles by the nitrate–citrate combustion method. Mater Res Bull. 2004;39:2249–2255.
[72] Li J, Wu Y, Pan Y, et al. Agglomeration of α-Al_2O_3 powders prepared by gel combustion. Ceram Int. 2008;34:1539–1542.
[73] Chen Q, Shi Y, Chen J, et al. Photoluminescence of Lu_2O_3:Eu^{3+} phosphors obtained by glycine-nitrate combustion synthesis. J Mater Res. 2005;20:1409–1414.
[74] Qi Z, Liu M, Chen Y, et al. Local structure of nanocrystalline Lu_2O_3:Eu studied by X-ray absorption spectroscopy. J Phys Chem C. 2007;111:1945–1950.
[75] Le Quang AQ, Zyss J, Ledoux I, et al. An hybrid organic-inorganic approach to erbium-functionalized nanodots for emission in the telecom window. Chem Phys. 2005;318:33–43.
[76] Pradal N, Potdevin A, Chadeyron G, et al. Structural, morphological and optical investigations on $BaMgAl_{10}O_{17}$:Eu^{2+} elaborated by a microwave induced solution combustion synthesis. Mater Res Bull. 2011;46:563–568.
[77] Ye T, Guiwen Z, Weiping Z, et al. Combustion synthesis and photoluminescence of nanocrystalline Y_2O_3:Eu phosphors. Mater Res Bull. 1997;32:501–506.
[78] Chen W, Li F, Yu J, et al. A facile and novel route to high surface area ceria-based nanopowders by salt-assisted solution combustion synthesis. Mater Sci Eng B. 2006;133:151–156.
[79] Deraz NM, Alarifi A. Novel processing and magnetic properties of hematite/maghemite nano-particles. Ceram Int. 2012;38:4049–4055.
[80] Lei Z, Zhu Q, Zhang S. Nanocrystalline scandia-doped zirconia (ScSZ) powders prepared by a glycine-nitrate solution combustion route. J Eur Ceram Soc. 2006;26:397–401.
[81] Bai J, Meng F, Wei C, et al. Solution combustion synthesis and characteristics of nanoscale MgO powders. Ceram Silik. 2011;55:20–25.
[82] Palneedi H, Mangam V, Das S, et al. Effect of fuel-to-nitrate ratio on the powder characteristics of nano-sized CeO_2 synthesized by mixed fuel combustion method. J Alloys Compd. 2011;509:9912–9918.
[83] Ranhan Sahu H, Ranga Rao G. Characterization of combustion synthesized zirconia powder by UV-vis, IR and other techniques. Bull Mater Sci. 2000;23:349–354.
[84] Toniolo JC, Lima MD, Takimi AS, et al. Synthesis of alumina powders by the glycine-nitrate combustion process. Mater Res Bull. 2005;40:561–571.
[85] Toniolo J, Takimi AS, Andrade MJ, et al. Synthesis by the solution combustion process and magnetic properties of iron oxide (Fe_3O_4 and α-Fe_2O_3) particles. J Mater Sci. 2007;42:4785–4791.
[86] Xu M, Yang L, Li Y, et al. Structural and magnetic properties of $Cu_{1-x}Mn_xO$ nanocrystal prepared by combustion synthesis. Phys B. 2011;406:3180–3186.
[87] Ahmadipour M, Venkateswara Rao K, Rajendar V. Formation of nanoscale Mg(x)Fe(1-x)O (x = 0.1, 0.2, 0.4) structure by solution combustion: effect of fuel to oxidizer ratio. J Nanomater. 2012;2012:163909.
[88] Chaiyo N, Muanghlua R, Niemcharoen S, et al. Solution combustion synthesis and characterization of lead-free piezoelectric sodium niobate ($NaNbO_3$) powders. J Alloys Compd. 2011;509:2445–2449.
[89] Chavan SV, Tyagi AK. Nanocrystalline $GdFeO_3$ via the gel-combustion process. J Mater Res. 2005;20:2654–2659.
[90] Grover V, Chavan SV, Sastry PU, et al. Combustion synthesis of nanocrystalline $Zr_{0.80}Ce_{0.20}O_2$: detailed investigations of the powder properties. J Alloys Compd. 2008;457:498–505.
[91] Jiang HQ, Endo H, Natori H, et al. Fabrication and photoactivities of spherical-shaped $BiVO_4$ photocatalysts through solution combustion synthesis method. J Eur Ceram Soc. 2008;28:2955–2962.
[92] Kuo CL, Chang YS, Chang YH, et al. Synthesis of nanocrystalline lithium niobate powders via a fast chemical route. Ceram Int. 2011;37:951–955.
[93] Khot VM, Salunkhe AB, Phadatare MR, et al. Formation, microstructure and magnetic properties of nanocrystalline $MgFe_2O_4$. Mater Chem Phys. 2012;132:782–787.
[94] Nagabhushana BM, Chakradhar RPS, Ramesh KP, et al. Effect of fuel on the formation structure, transport and magnetic properties of $LaMnO_{3+}$ nanopowders. Philos Mag. 2010;90:2009–2025.
[95] Salunkhe AB, Khot VM, Phadatare MR, et al. Combustion synthesis of cobalt ferrite nanoparticles-influence of fuel to oxidizer ratio. J Alloys Compd. 2012;514:91–96.
[96] Ahmed MA. The effect of urea-to-nitrates ratio on the morphology and magnetic properties of $Mn_{0.8}Mg_{0.2}Fe_2O_4$. J Magn Magn Mater. 2010;322:763–766.
[97] Chien RR, Tu CS, Schmidt VH, et al. Synthesis and characterization of proton-conducting $Ba(Zr_{0.8-x}Ce_xY_{0.2})O_{2.9}$ ceramics. Solid State Ionics. 2010;181:1251–1257.

[98] Deganello F, Marci G, Deganello G. Citrate-nitrate auto-combustion synthesis of perovskite-type nanopowders: a systematic approach. J Eur Ceram Soc. 2009;29:439–450.
[99] Epherre R, Duguet E, Mornet S, et al. Manganite perovskite nanoparticles for self-controlled magnetic fluid hyperthermia: about the suitability of an aqueous combustion synthesis route. J Mater Chem. 2011;21:4393–4401.
[100] Kikukawa N, Takemori M, Nagano Y, et al. Synthesis and magnetic properties of nanostructured spinel ferrites using a glycine-nitrate process. J Magn Magn Mater. 2004;284:206–214.
[101] Vijayan L, Cheruki R, Govindaraj G, et al. Physical and electrical properties of combustion synthesized NASICON type $Na_3Cr_2(PO_4)_3$ crystallites: effect of glycine molar ratios. Mater Chem Phys. 2011;130:862–869.
[102] Verma S, Joy PA, Kurian S. Structural, magnetic and mössbauer spectral studies of nanocrystalline $Ni_{0.5}Zn_{0.5}Fe_2O_4$ ferrite powders. J Alloys Compd. 2011;509:8999–9004.
[103] Biamino S, Fino P, Pavese M, et al. Alumina–zirconia–yttria nanocomposites prepared by solution combustion synthesis. Ceram Int. 2006;32:509–513.
[104] Bianchetti MF, Juárez RE, Lamas DG, et al. Synthesis of nanocrystalline CeO_2-Y_2O_3 powders by a nitrate-glycine gel-combustion process. J Mater Res. 2002;17:2185–2188.
[105] Rasouli S, Danaee I. Effect of preparation method on the anti-corrosive properties of nanocrystalline Zn-CoO ceramic pigments. Mater Corros. 2011;62:405–410.
[106] Weil SK, Hardy JS. Use of combustion synthesis in preparing ceramic-matrix and metal-matrix composite powders. Ceram Eng Sci Proc. 2004;25:159–164.
[107] Chen W, Li F, Yu J, et al. Rapid synthesis of mesoporous ceria-zirconia solid solutions via a novel salt-assisted combustion process. Mater Res Bull. 2006;41:2318–2324.
[108] Samantaray S, Mishra BG, Pradhan DK, et al. Solution combustion synthesis and physicochemical characterization of ZrO_2-MoO_3 nanocomposite oxides prepared using different fuels. Ceram Int. 2011;37:3101–3108.
[109] Valefi M, Falamaki C, Ebadzadeh T, et al. New insights of the glycine-nitrate process for the synthesis of nano-crystalline 8YSZ. J Am Ceram Soc. 2007;9:2008–2014.
[110] Zhuravlev VD, Vasil'ev VG, Vladimirova EV, et al. Glycine-nitrate combustion synthesis of finely dispersed alumina. Glass Phys Chem. 2010;36:506–512.
[111] Yang W, Zhang G, Xie J, et al. A combustion method to prepare spinel phase $LiMn_2O_4$ cathode materials for lithium-ion batteries. J Power Sources. 1999;81-82:412–415.
[112] Sahoo P, Misra DK, Salvador J, et al. Microstructure and thermal conductivity of surfactant-free NiO nanostructures. J Solid State Chem. 2012;190:29–35.
[113] Hyppänen I, Hölsä J, Kankare J, et al. Up-conversion luminescence properties of Y_2O_2S:Yb_{3+}, Er_{3+} nanophosphors. Opt Mater. 2009;31:1787–1790.
[114] Ta N, Chen D. Combustion synthesis of β-$Ca_{1.95}P_2O_7$:$0.05Eu^{2+}$ blue phosphor for near ultraviolet excitation. J Alloy Compd. 2009;484:514–518.
[115] Rodrigues L, Stefani R, Brito H, et al. Thermoluminescence and synchrotron radiation studies on the persistent luminescence of $BaAl_2O_4$:Eu^{2+},Dy^{3+}. J Solid State Chem. 2010;183:2365–2371.
[116] Chen W, Hong J, Li Y. Facile fabrication of perovskite single-crystalline $LaMnO_3$ nanocubes via a salt-assisted solution combustion process. J Alloy Compd. 2009;484:846–850.
[117] Tong Y, Zhao S, Wang X, et al. Synthesis and characterization of $Er_2Sn_2O_7$ nanocrystals by salt-assistant combustion method. J Alloy Compd. 2009;479:746–749.
[118] Tong Y, Zhang R, Zhao S, et al. A convenient method for preparing well-dispersed $Er_2Zr_2O_7$ nanocrystals. Adv Mater Res. 2010;123–125:611–614.
[119] Zhang X, Jiang W, Song D, et al. Salt-assisted combustion synthesis of highly dispersed superparamagnetic $CoFe_2O_4$ nanoparticles. J Alloy Compd. 2009;475:L34–L37.
[120] Manjunatha C, Nagabhushana B, Sunitha D, et al. Influence of halide flux on the crystallinity, microstructure and thermoluminescence properties of $CdSiO_3$:Co^{2+} nanophosphor. Mater Res Bull. 2013;48:158–166.
[121] Ramakrishna G, Nagabhushana H, Prashantha SC, et al. Role of flux on morphology and luminescence properties of Sm^{3+} doped Y_2SiO_5 nanopowders for WLEDs. Spectrochim Acta A. 2015;136:356–365.
[122] Chen Z, Hong X, Yan YW. Morphology and luminescence performance of the nano-sized $BaMgAl_{10}O_{17}$:Eu^{2+} phosphor with PEG as additive. J Synth Cryst. 2006;35:1277–1282.
[123] Burgos-Montes O, Moreno R, Colomer MT, et al. Synthesis of mullite powders through a suspension combustion process. J Am Ceram Soc. 2006;89:484–489.
[124] Civera A, Pavese M, Saracco G, et al. Combustion synthesis of perovskite-type catalysts for natural gas combustion. Catal Today. 2003;83:199–211.
[125] Yao SS, Li YY, Xue LH, et al. Combustion synthesis and luminescent properties of a blue-green emitting phosphor: ($Ba_{1.95}$, $Eu_{0.05}$)$ZnSi_2O_7$:B_{3+}. Cent Eur J Phys. 2009;7:800–805.
[126] Takeda T, Koshiba D, Kikkawa S. Gel combustion synthesis of fine crystalline $(Y_{0.95}Eu_{0.05})_2O_3$ phosphor in presence of lithium flux. J Alloy Compd. 2006;408-412:879–882.
[127] Peng T, Liu X, Dai K, et al. Effect of acidity on the glycine–nitrate combustion synthesis of nanocrystalline alumina powder. Mater Res Bull. 2006;41:1638–1645.
[128] Patra H, Rout SK, Pratihar SK, et al. Effect of process parameters on combined EDTA–citrate synthesis of $Ba_{0.5}Sr_{0.5}Co_{0.8}Fe_{0.2}O_{3-\delta}$ perovskite. Powder Technol. 2011;209:98–104.
[129] Mohebbi H, Ebadzadeh T, Hesari F. Synthesis of nano-crystalline (Ni/NiO)–YSZ by microwave-assisted combustion synthesis method: the influence of pH of precursor solution. J Power Sources. 2008;178:64–68.
[130] Zavala LA, Fernández P, Novitskaya E, et al. Interconfigurational and intraconfigurational transitions of Yb^{2+} and Yb^{3+} ion in hydroxyapatite: a cathodoluminescence study. Acta Mater. 2017;135:35–43.
[131] Thoda O, Xanthopoulou G, Vekinis G, et al. Review of recent studies on solution combustion synthesis of nanostructured catalysts. Adv Eng Mater. 2018;20:1800047.
[132] Hossain MK, Kecsenovity E, Varga A, Molnár M, Janáky C, Rajeshwar K. Solution combustion synthesis of complex oxide semiconductors. Int J Self Propag High Temp Synth. 2018;27:129–140.

[133] Deganello F, Tyagi AK. Solution combustion synthesis, energy and environment: best parameters for better materials. Prog Cryst Growth Charact Mater. 2018;64:23–61.
[134] Cahill JT, Graeve OA. Hexaborides: a review of structure, synthesis and processing. J Mater Res Technol. 2019;8:6321–6335.
[135] Graeve OA, Yazdani A, Kelly JP, et al. Effect of SiO_2 on the sintering of cerium-doped lutetium oxyorthosilicate. Opt Mater. 2020;100:109650.
[136] Motloung SJ, Lephoto MA, Tshabalala KG, et al. Combustion synthesis and characterization of $MV_{0.5}P_{0.5}O_4$:Sm_{3+},Tm_{3+} (M = Gd, La, Y). Phys B. 2018;535:211–215.
[137] Maji D, Ananthasivan K, Venkata Krishnan R, et al. Nanocrystalline $(U_{0.5}Ce_{0.5})O_{2\pm x}$ solid solutions through citrate gel-combustion. J Nucl Mater. 2018;502:370–379.
[138] Vieten J, Bulfin B, Roeb M, et al. Citric acid auto-combustion synthesis of Ti-containing perovskites via aqueous precursors. Solid State Ionics. 2018;315:92–97.
[139] Pujar P, Vardhan RV, Gupta D, et al. A balancing between super transparency and conductivity of solution combustion derived titanium doped indium oxide: effect of charge carrier density and mobility. Thin Solid Films. 2018;660:267–275.
[140] Xuan H, Xu Y, Zhang Y, et al. One-step combustion synthesis of porous CNTs/C/$NiMoO_4$ composites for high-performance asymmetric supercapacitors. J Alloys Compd. 2018;745:135–146.
[141] Ardebilchi Marand N, Masoudpanah SM, Bagfhi MS, et al. Photocatalytic activity of nickel sulfide composite powders by solution combustion method. J Electron Mater. 2020;49:1266–1272.
[142] Ardebilchi Marand N, Masoudpanah SM, Bafghi MS. Solution combustion synthesis of nickel sulfide composite powders. Ceram Int. 2018;44:17277–17282.
[143] Zahiri M, Afarani MS, Arabi AM. Dual functions of thiourea for solution combustion synthesis of ZnO/ZnS composite powders: fuel and sulphur source. Appl Phys A. 2018;124:663.